https://doi.org/10.1093/brain/awac083 BRAIN 2022: 145; 2849–2868 | 2849

BRAIN
ORIGINAL ARTICLE

Microglial large extracellular vesicles propagate early synaptic dysfunction in Alzheimer's disease

Martina Gabrielli,[1] Ilaria Prada,[1] Pooja Joshi,[1] Chiara Falcicchia,[2] Giulia D'Arrigo,[1] Grazia Rutigliano,[3,4] Elisabetta Battocchio,[1,5] Rossella Zenatelli,[6] Francesca Tozzi,[7] Annalisa Radeghieri,[6,8] Ottavio Arancio,[9,10,11] Nicola Origlia[2] and Claudia Verderio[1]

Synaptic dysfunction is an early mechanism in Alzheimer's disease that involves progressively larger areas of the brain over time. However, how it starts and propagates is unknown.

Here we show that amyloid-β released by microglia in association with large extracellular vesicles (Aβ-EVs) alters dendritic spine morphology *in vitro*, at the site of neuron interaction, and impairs synaptic plasticity both *in vitro* and *in vivo* in the entorhinal cortex–dentate gyrus circuitry. One hour after Aβ-EV injection into the mouse entorhinal cortex, long-term potentiation was impaired in the entorhinal cortex but not in the dentate gyrus, its main target region, while 24 h later it was also impaired in the dentate gyrus, revealing a spreading of long-term potentiation deficit between the two regions. Similar results were obtained upon injection of extracellular vesicles carrying Aβ naturally secreted by CHO7PA2 cells, while neither $A\beta_{42}$ alone nor inflammatory extracellular vesicles devoid of Aβ were able to propagate long-term potentiation impairment. Using optical tweezers combined to time-lapse imaging to study Aβ-EV–neuron interaction, we show that Aβ-EVs move anterogradely at the axon surface and that their motion can be blocked through annexin-V coating. Importantly, when Aβ-EV motility was inhibited, no propagation of long-term potentiation deficit occurred along the entorhinal–hippocampal circuit, implicating large extracellular vesicle motion at the neuron surface in the spreading of long-term potentiation impairment.

Our data indicate the involvement of large microglial extracellular vesicles in the rise and propagation of early synaptic dysfunction in Alzheimer's disease and suggest a new mechanism controlling the diffusion of large extracellular vesicles and their pathogenic signals in the brain parenchyma, paving the way for novel therapeutic strategies to delay the disease.

1 CNR Institute of Neuroscience, Vedano al Lambro, MB 20854, Italy
2 CNR Institute of Neuroscience, Pisa 56124, Italy
3 Institute of Life Sciences, Sant'Anna School of Advanced Studies, Pisa 56127, Italy
4 CNR Institute of Clinical Physiology, Pisa 56124, Italy
5 School of Medicine and Surgery, University of Milano-Bicocca, Monza 20900, Italy
6 Department of Molecular and Translational Medicine, University of Brescia, Brescia 25123, Italy
7 Bio@SNS Laboratory, Scuola Normale Superiore, Pisa, 56124, Italy
8 Consorzio Sistemi a Grande Interfase (CSGI), Department of Chemistry, University of Florence, Sesto Fiorentino, FI 50019, Italy
9 Department of Pathology and Cell Biology, Columbia University, New York, NY 10032, USA
10 The Taub Institute for Research on Alzheimer's Disease and the Aging Brain, Columbia University, New York 10032, NY, USA
11 Department of Medicine, Columbia University, New York, NY 10032, USA

Received June 02, 2021. Revised January 17, 2022. Accepted February 13, 2022. Advance access publication March 3, 2022

Correspondence to: Claudia Verderio
CNR Institute of Neuroscience via Raoul Follereau 3, Vedano al Lambro MB, 20854, Italy
E-mail: c.verderio@in.cnr.it

Correspondence may also be addressed to: Nicola Origlia
CNR Institute of Neuroscience, via Moruzzi 1 Pisa, 56124, Italy
E-mail: origlia@in.cnr.it

Keywords: microglia; extracellular vesicles; amyloid-beta; Alzheimer's disease; long-term potentiation

Abbreviations: Aβ = amyloid-β; DG = dentate gyrus; EC = entorhinal cortex; EV = extracellular vesicle; HFS = high-frequency stimulation; LTP = long-term potentiation; mEPSC = miniature excitatory post-synaptic current; PP = perforant pathway; RFP = red fluorescent protein; TRPS = tunable resistive pulse sensing

Introduction

Alzheimer's disease is a progressive degenerative encephalopathy characterized by loss of memory and reasoning, profound behavioural disorders and personality changes, leading to dementia and death. Neuropathological hallmarks of the disease are loss of synapses and neurons, extracellular amyloid-β (Aβ) deposition and intraneuronal tau aggregation.[1] Activation of microglia, the immune cells of the brain, is an additional feature of the disease.[2]

It has been proposed that Alzheimer's pathology originates in specific areas of the brain and then spreads to progressively larger regions over time, following an anatomically defined pattern of connections.[3–8] Extensive literature identifies synaptic dysfunction as an early mechanism affected in the disease,[9–13] which correlates with cognitive decline.[12,14] However, how synaptic dysfunction originates and propagates in the affected brain is still largely obscure, and it is now one of the most compelling questions in Alzheimer's disease research.

Amyloid-β_{42} has been long related to Alzheimer's disease pathogenesis as a key factor (for an exhaustive review see Selkoe and Hardy, 2016[10]). In its toxic oligomeric form,[15,16] $A\beta_{42}$ is able to profoundly alter synaptic function, typically affecting synaptic plasticity and ultimately leading to synapse loss.[9,15,17–21]

The circuit connecting the entorhinal cortex (EC) to the dentate gyrus (DG) of the hippocampus *via* the perforant path (PP) represents a useful model to study synaptic dysfunction and its propagation in the early disease stages. In fact, the entorhinal–hippocampal circuit plays a pivotal role in various forms of memory including episodic memory,[22,23] typically impaired in Alzheimer's patients, and is one of the most vulnerable and early affected regions in the disease.[24–26] According to an MRI longitudinal study, the EC, followed by the hippocampal formation, are the brain regions showing the first morphological alterations in Alzheimer's disease, well before the clinical onset.[27] Significant loss of neurons occurs in EC layer II at early pathological stages,[28] and this deficit is associated with synaptic loss in the hippocampal regions receiving PP afferent input in subjects with mild cognitive impairment.[29] Irrespective of the primary site of origin of Alzheimer's disease, studies support the hypothesis that EC is a source of Aβ in the mouse hippocampus: lesions of the EC or transecting the PP reduce Aβ accumulation in the DG of transgenic APP/PS1 mice.[30,31] Interestingly, it has been reported that prevalent overexpression of mutant amyloid precursor protein (APP)/Aβ in the EC mediates trans-synaptic propagation of Aβ-induced neuronal dysfunction from the EC to the hippocampus, up to altering cortical network activity, and elicits Alzheimer-like behavioural deficits in mice.[13]

Recent advances in genetic and transcriptomic studies have pointed to microglia-related pathways as central to Alzheimer's disease risk and pathogenesis.[32–37] Neuroinflammation occurs early in Alzheimer's disease,[38,39] with microgliosis even preceding plaque formation,[40] suggesting an unexpected pathological role for microglia in the first stages of the disease. A few mechanisms have been involved in Alzheimer's disease pathogenesis by inappropriately activated microglia: excessive synaptic pruning[41] and release of synaptotoxic Aβ/tau in association with extracellular vesicles (EVs).[42–46]

Extracellular vesicles are a heterogeneous population of membrane vesicles formed at the plasma membrane (ectosomes/microvesicles) or in the endocytic compartment (exosomes), which contain and transfer cellular components from a donor to a recipient cell.[47–49] Importantly EV cargo includes pathological proteins such as Aβ, which is stored both in the EV lumen and at the EV surface.[42,43,50,51] Given the difficulties in partitioning EVs into microvesicles and exosomes without cross-contamination, they are now preferentially classified by size and other physical characteristics (density, biochemical composition) into small (≤100–200 nm diameter) and large (>200 nm diameter) EVs.[52] Despite a previous study showed that microglial production of large EVs carrying synaptotoxic Aβ species (Aβ-EVs) correlates with early brain damage in prodromal Alzheimer's disease,[53] whether and how this less-studied EV population contributes to initial synaptic dysfunction remains elusive.

In this study, we sought to investigate whether large Aβ-EVs produced by microglia impair synaptic plasticity and propagate synaptic dysfunction by moving at the axon surface. This hypothesis has been suggested by our recent work indicating that large astrocyte-derived EVs use neurites as routes to move extracellularly among connected neurons.[54] We show that large microglial Aβ-EVs affect synaptic plasticity both in culture and in slices and, once injected in the mouse brain, propagate synaptic dysfunction in the entorhinal–hippocampal circuit through a mechanism sensitive to annexin-V, a phosphatidylserine ligand blocking EV extracellular motion.

Materials and methods

Animals

C57BL/6 E18-19 mouse embryos, postnatal Day 2 (P2) newborn and adult mice (purchased from Charles River) were employed. All experimental procedures involving animals followed the guidelines defined by European legislation (Directive 2010/63/EU) and Italian Legislation (LD no. 26/2014). The Organism Responsible for

Animal Welfare (OPBA) of National Research Council of Italy (CNR) Institute of Neuroscience in Milan-Pisa and the Italian Ministry of Health approved the study protocols (authorizations 2D46A.N.KBG and 233/2019-PR).

Primary cultures

Mixed glial cultures were established from P2 C57BL/6 mice of either sex (Charles River), while hippocampal neurons were established from the hippocampi of C57BL/6 E18-19 mouse embryos of either sex (Charles River), as previously described.[55] See Supplementary material.

Amyloid-β treatment

Microglia primary cultures were exposed to 2 μM human $A\beta_{42}$ (reconstituted in DMSO; cat. AS-20276, AnaSpec, Eurogentec) for 20 h, as previously described.[42]

CHO7PA2 conditioned medium

CHO7PA2 cells are Chinese hamster ovary (CHO) cell lines stably transfected with human APP_{751} bearing the Val717Phe mutation (7PA2 cells). Transfected cells were kindly gifted by Dr. Selkoe (Harvard Medical School, Boston, MA, USA) and maintained according to Podlisny *et al.*[56] CHO7PA2 conditioned medium, containing Aβ species at nanomolar concentrations, was collected according to Podlisny *et al.*[56] See Supplementary material.

Immunostaining of microglia-internalized amyloid-β

Immunostaining of microglia-internalized Aβ was performed as in Joshi *et al.*,[42] using 1:100 Isolectin GS-IB4 from *Griffonia simplicifolia*, Alexa Fluor™ 568 conjugate (Invitrogen # I21412, Thermo Fisher Scientific) on living cells and 6E10 mouse anti-β-amyloid 1–16 antibody (1:100; Biolegend, previously Covance cat. #SIG-39300) after fixation. See also Supplementary material.

Extracellular vesicle isolation

Large EV-enriched samples were isolated through differential centrifugation, upon ATP stimulation in a physiological solution (Krebs–Ringer HEPES solution, KRH) following a protocol fine-tuned in the laboratory.[55] See also Supplementary material.

Western blotting

Western Blotting was performed as in Prada *et al.*,[57] using rabbit anti-Alix (1:500; Covalab), mouse anti-Flotillin (1:1000, BD Biosciences), rabbit anti-Annexin A2 (1:5000, Abcam), rabbit anti-GAPDH (1:1000, #247002, Synaptic Systems), mouse anti-GS28 (1:1000; BD Biosciences), rabbit anti-TOM20 (1:500; Santa Cruz Biotechnology) and mouse anti-Aβ 6E10 (1:1000; Biolegend, previously Covance cat. #SIG-39300). See also Supplementary material.

Colorimetric nanoplasmonic assay

Extracellular vesicle preparations from $A\beta_{42}$-treated microglia and control cells were characterized for purity from contaminants, referred to as co-separated soluble exogenous single and aggregated proteins, with the colorimetric nanoplasmonic (CONAN) assay, following the open-access protocol by Zendrini *et al.*[58] See Supplementary material.

Extracellular vesicle characterization by tunable resistive pulse sensing

Tunable resistive pulse sensing (TRPS) using the Izon qNano instrument (Izon) was carried out to measure the size distribution and concentration of 10 000*g* (large) Aβ-EV fractions, as well as their surface charge. See also Supplementary material.

Amyloid-β quantification in extracellular vesicles

Quantitative determination of $A\beta_{42}$ in EVs was performed using Human Aβ42 enzyme-linked immunosorbent assay (ELISA) Kit (Invitrogen cat. KHB3441, Thermo Fisher Scientific). Aβ-EV pellets [10 000*g* (large)] were resuspended in Standard Diluent Buffer from the kit, supplemented with 1:100 Halt Protease Inhibitor (Thermo Fisher Scientific) and 1 mM phenylmethylsulfonyl fluoride (PMSF, Merck). Lysed EV samples were solubilized with 0.57% Triton X-100 (Merck) followed by 20 s vortexing (as described by Bianco *et al.*[59] and Osteikoetxea *et al.*[60]). The assay was performed according to the manufacturer's protocol. Halt Protease Inhibitor, PMSF and Triton X-100 were added to Aβ standards at the same concentration as in the samples. Absorbance was detected at 450 nm using a Wallac 1420 Multilabel Counter—Victor2 (Perkin-Elmer).

Cryo-electron microscopy of extracellular vesicles

Freshly prepared 10 000*g* (large) Aβ-EV pellets resuspended in saline were plunge frozen in liquid ethane using a Vitrobot Mk IV (Thermo Fisher Scientific). Images of the vitrified specimen were acquired using a Talos Arctica transmission electron microscope (Thermo Fisher Scientific). See also Supplementary material.

Annexin-V treatment

A 10 000*g* (large) Aβ-EV pellet was resuspended in 300 μl KRH (in mM, 125 NaCl, 5 KCl, 1.2 $MgSO_4$, 1.2 KH_2PO, 2 $CaCl_2$, 6 D-glucose, 25 HEPES/NaOH, pH 7.4) and annexin-V (A7810, Merck) was added at an active concentration of 8.4 μg/ml for 30 min on a low-speed wheel at room temperature. Subsequently, 1 ml KRH was added to the sample to dilute the molecule and EVs were re-pelleted at 10 000*g* for 30 min at 4°C.

Optical tweezer experiments

Optical trapping and manipulation of EVs was performed following the approach previously described.[54,61] In order to distinguish dendrites from axons, 12×10^4 neurons on 24 mm glass coverslips were transfected with RFP (red fluorescent protein) using Lipofectamine 2000 (Invitrogen, Thermo Fisher Scientific). Before recording, neurons were washed to remove EVs constitutively released by neurons and large-EVs (10 000*g* pellet) produced by $\sim 1 \times 10^5$ microglia were added to neurons and maintained in 500 μl of phenol red-free neuronal medium in a 5% CO_2 and temperature-controlled recording chamber at 37°C. See also Supplementary material.

Dendritic spine analysis

Neurons [14–17 days in vitro (DIV), 12×10^4 (on 24 mm glass coverslips)] were imaged with a 63× objective using an Axiovert 200 M equipped with spinning disk microscope prior and 2, 10, 20, 30 and 40 min after placing single EV on an RFP-positive dendrite through optical manipulation. Acquisition software was Volocity 6.3.0 (Perkin Elmer). Analysis was performed only when the EV adhered to the dendrite. Focal planes were stacked together in a

maximum intensity projection and RFP-positive spines were analysed in the vicinity of the EV contact site (<7 μm from the contact point), far from the contact site (>60 μm from the contact point) or along the entire dendrite. Spine morphology was analysed using ImageJ software (http://imagej.nih.gov/ij/). Spines were classified in categories (mushroom, thin, stubby) based on morphological parameters: spine head diameter (H), spine length (L) and spine neck width (N), according to NeuronStudio software criteria, as in Prada *et al.*[57]

Tracking of single extracellular vesicles on neurons

After placing the EV on neurons (13–17 DIV), cells were live imaged using a digital camera (high-sensitivity USB 3.0 CMOS Camera 1280 × 1024 Global Shutter Monochrome Sensor, Thorlabs) at a frame rate of 2 Hz for 40 min. Videos were saved as *.AVI files for offline analysis. EV position was determined for each video frame (considering two frames every 5 s) using a custom MATLAB code (it.mathworks.-com). To evaluate EV displacement on the neuron process, two distances were calculated: the length of the path travelled by the EV in the first 10 min after contact (pathlength) and the maximum distance covered by the EV from the contact point in both direction in the first 10 min after contact (sum of distances reached by the EV in both directions). Mean velocity and distances were extracted from EV coordinates using a custom R code (www.r-project.org) that exploits the Pythagorean theorem to reconstruct the EV path point-to-point. We classified as 'static EVs' (i) the EVs with net displacement < of the EV diameter; and (ii) EVs showing only random (Brownian) motion.

Subcellular localization of large mCLING-labelled extracellular vesicles

Labelling of EVs with mCLING was performed according to Brenna *et al.*[62] Briefly, EVs in the 10 000*g* pellet were resuspended in 500 μl of sterile and 0.1 μm filtered PBS and incubated with 400 nM mCLING-ATTO 647N-labelled (Synaptic Systems) in a black tube on ice for 5 min. The reaction was quenched by adding 500 μl of 1% BSA in PBS. Then, EVs were diluted in 10 ml of PBS, re-pelleted at 10 000*g* to eliminate the dye excess, resuspended in neuronal medium and added to membrane-targeted GFP-transfected hippocampal neurons for 1 h before fixing the cells with 4% paraformaldehyde–4% sucrose (w/v) for 8 min. Coverslips were then mounted on a microscope slide and Z-stacks were acquired with a Zeiss LSM800 confocal microscope. Analysis of EV localization on axons was performed on ImarisViewer 9.7.2.

Immunofluorescence analysis of juxtaposed pre-/post-synaptic puncta

Neurons (8×10^4 on 24 mm coverslips) were incubated with 0.6×10^8/ml EVs for 3 h, then fixed with 4% paraformaldehyde–4% sucrose (w/v) and stained with guinea-pig anti-Bassoon (Synaptic Systems, Cat# 141 004, RRID:AB_2290619) and rabbit anti-Shank-2 (Synaptic Systems Cat# 162 202, RRID:AB_2619860) primary antibodies, followed by Alexa-555 and Alexa-488 secondary antibodies (1:200, Alexa, Invitrogen). Analysis was performed according to Prada *et al.*[57] See Supplementary material.

Electrophysiology on cell culture

Mature hippocampal neurons (7×10^4 in culture on 15 mm coverslips) were incubated with 2×10^7 ctrl-EVs or Aβ-EVs in 330 μl, or vehicle, for 1 h. To record miniature excitatory post-synaptic currents (mEPSCs), the voltage-gated Na^+-channel blocker tetrodotoxin (TTX, 0.5 μM, Alomone Labs) and the GABA-A receptor antagonist picrotoxin (100 μM, Merck) were added to the bath solution, along with strychnine (1 μM, Merck), used to avoid glycine receptor activation. In order to investigate synaptic plasticity, after 12 min baseline recording in standard bath solution, Mg^{2+}-free bath solution was perfused for 1 min before applying the same solution containing glycine (Gly, 200 μM, Merck) for 3 min. Subsequently, perfusion was resumed with standard Mg^{2+}-containing bath solution and recording continued for 40 min. Potentiation magnitude was measured as the average response between the 28th and the 40th min after glycine. See also Supplementary material.

Stereotaxic entorhinal cortex injection

For stereotaxic injections, 2–3-month-old C57BL/6 mice (male and female in equal number) were deeply anaesthetized using urethane (Merck, 20% solution, 0.1 ml/100 g of body weight) *via* intraperitoneal injection. After tail pinch reflex disappearance, mice were positioned in a stereotaxic apparatus. The scalp was shaved and a midline incision was made. Two holes were drilled bilaterally at stereotaxic coordinates targeting the lateral EC (AP −3.8 mm, ML ±4.0 mm from Bregma, measured on the skull surface). An injecting needle was then inserted through the holes and 1 μl of EVs [0.25×10^8/μl or 0.11×10^8/μl in artificial CSF (ACSF)], soluble oligomeric $A\beta_{42}$ alone (100 nM in ACSF; prepared as previously described[63]) or ACSF alone (vehicle) was slowly injected 4 mm below the dura. ACSF composition was the following (in mM): 119 NaCl, 2.5 KCl, 2 $CaCl_2$, 1.2 $MgSO_4$, 1 NaH_2PO_4, 6.2 $NaHCO_3$, 10 glucose, 10 HEPES. The pipette remained in place at the injection site for 2 min before slow removal. Then, the scalp was sutured and the mouse was brought back to its cage for recovery.[64]

Slice preparation

One hour or 24 h after EC injection, animals were sacrificed and EC/hippocampal slices were cut as described.[65] See Supplementary material.

Electrophysiology in slices

Extracellular field potentials and whole cell patch-clamp recordings were performed as previously described.[65,66] See Supplementary material.

Statistical analysis

Statistical analysis was performed using SigmaStat 3.5 for Windows (Systat Software Inc., San Jose, CA, USA). A normality test was performed for all data sets and the proper statistical test was selected accordingly. Two-tailed statistical tests have been performed if not otherwise stated. Data are shown as mean ± SEM. Optical tweezer data of adhering/moving EVs are expressed as raw percentage on total tested EVs (i.e. total number of EVs placed on axons, no average) and analysed by chi-square test. Chi-square is the appropriate statistical test to compare raw percentages, to determine if there is a significant difference in the distribution of a group among different categories beyond what can be attributed to random sampling variation (e.g. for EVs, categories were: adhered/did not adhere, moved/did not move). Differences were considered significant when $P < 0.05$ and indicated by

asterisks: *P < 0.05, **P < 0.01, ***P < 0.001. *n* indicates the number of measurements taken from distinct samples. A *priori* sample size calculations have been performed using G*Power 3 software (Heinrich Heine Universität, Düsseldorf, Germany). See also Supplementary material.

Data availability

The data that support the findings of this study are available from the corresponding authors upon reasonable request. The R custom code used for EV analysis is available at https://doi.org/10.6084/m9.figshare.12808211.v1.

Results

Isolation of large Aβ-EV enriched fraction and characterization

Primary murine microglia were exposed to 2 μM exogenous $A\beta_{42}$ for 20 h to allow $A\beta_{42}$ internalization and then were activated with 1 mM ATP to stimulate the release of EVs carrying Aβ forms (Aβ-EVs), as previously characterized.[42,43] Samples enriched in large Aβ-EVs or large ctrl-EVs, released by microglia not exposed to $A\beta_{42}$, were isolated according to MISEV2018 guidelines,[52] by differential centrifugation at 10 000*g* after pre-clearing of cell supernatant from cells and debris at 300*g*, as previously established in our laboratory.[42,55]

Western blotting analysis indicated that large microglial EVs released upon short (up to 1 h) stimulation with ATP and isolated by differential centrifugation are positive for the EV markers flotillin 1, alix and annexin-A2, a typical marker of large EVs, and almost unstained for intracellular organelle markers (GS28 and TOM20 for Golgi and mitochondria, respectively) or the cytosolic marker GAPDH (Fig. 1A and Supplementary Fig. 1 for normalization to total proteins). As expected, Aβ-EVs contained Aβ, as indicated by positive staining for anti-Aβ 6E10 antibody, with Aβ being highly enriched in EVs compared with donor cells (about 10-fold change, Fig. 1A). The purity of EV preparations was corroborated by analysis with the CONAN assay, which consists of a solution of gold nanoparticles (AuNPs) into which EVs are added. The solution turns blue if the EV preparation is pure, whereas it stays red if protein contaminants are present. Quantification of the colour change provides an aggregation index (AI), which is an index of purity. Results reported in Fig. 1B show that both the EV preparations from $A\beta_{42}$-treated microglia and control cells reach AI lower than 20%, indicating that in both samples contaminants are below 0.05 μg/μl[58] (Fig. 1B).

Large Aβ-EV enriched fractions were highly heterogeneous in size, ranging from 92 nm to 1.7 μm as indicated by TRPS analysis (Fig. 1C). Large Aβ-EVs had a mean size of 315.00 ± 5.68 nm, with a mode of 140.00 nm. According to this method, the percentage of large EVs above 200 nm was ∼59%. Aβ-EV production was rated to $\sim 0.5 \times 10^8$ EVs ($4.66 \times 10^7 \pm 1.55 \times 10^7$; $n = 4$) from 1 million cells in 1 h, similar to microglia not exposed to Aβ.[57]

Following EV solubilization with 0.57% Triton X-100[59,60] and ELISA $A\beta_{42}$ measurement, we found that 0.5×10^8 large Aβ-EVs isolated at 10 000*g* contain ∼370 pg of $A\beta_{42}$. A similar amount of Aβ was detected in small Aβ-EVs pelleted at 100 000*g* (∼330 pg). Half of the amount of $A\beta_{42}$ was detected in intact Aβ-EVs, not treated with the detergent, in the large EV-enriched fraction (Fig. 1E), suggesting that Aβ is located both in the lumen and at the outer surface of Aβ-EVs, as previously described.[42,43,50,51] Consistent with the presence of Aβ species enriched in negatively charged residues[67] at the EV surface, Z-potential analysis revealed a significant negative shift in the surface charge compared to ctrl-EVs (produced by microglia not exposed to Aβ; −22.57 mV Aβ-EVs versus −10.75 mV ctrl-EVs; Fig. 1D). Interestingly, $A\beta_{42}$ content in large EVs-enriched fraction rose significantly when microglia were exposed to Bafilomycin A1 (25 nM) to block intracellular degradative pathways (Fig. 1F), indicating a role for EVs in Aβ disposal. EV production was not affected by Bafilomycin treatment (Fig. 1G). Large Aβ-EVs enriched fraction was further characterized by cryo-electron microscopy, which confirmed large heterogeneity in vesicle size and morphology (Fig. 1H). Most Aβ-EVs were unilamellar, round and with a smooth surface, but we observed examples of multilamellar and tubular vesicles (Fig. 1H, arrows and white arrowheads, respectively) or with rough surface (Fig. 1H, black arrowheads).

Collectively, these findings showed that large EVs are highly enriched in Aβ species generated from $A\beta_{42}$ internalized in microglia and confirmed that part of $A\beta_{42}$ is exposed on the EV surface. Because large Aβ-EVs can be monitored by bright field microscopy, in this study we focused on this population of less-studied EVs to analyse their impact on synaptic morphology and function.

Large Aβ-EVs affect dendritic spine morphology and synaptic plasticity *in vitro*

Dendritic spines are post-synaptic elements of excitatory neurons, whose size is correlated with synapse strength, hinting at a possible structural mechanism at the basis of synaptic plasticity.[68] To explore the possible contribution of Aβ-EVs to synaptic dysfunction, we first characterized the action of large Aβ-EVs on dendritic spine density and morphology. This investigation was performed on cultured hippocampal neurons using optical tweezers, an innovative technique that allows to gently placing single EV on the cell surface,[61] mimicking the random attachment of EVs to cultured neurons.[55]

Neurons were transfected with cytoplasmic RFP to delineate the spine shape and time-lapse imaged by spinning disk microscopy prior and 2, 10, 20, 30 and 40 min after the contact of large Aβ-EVs or ctrl-EVs with secondary dendrites (Fig. 2A). Briefly, confocal images of RFP-positive dendrites were first acquired. Then, in bright-field, a small amount of large EVs ($\sim 0.5 \times 10^7$) was loaded into the medium and a single large EV was trapped and finely placed onto the selected dendrite by optical manipulation. EVs > 200 nm, above the resolution limit, were more easily visualized in bright-field and manipulated by the laser trap. After 30 s, the laser tweezers were switched off and EV adhesion to the cell surface monitored. Only when EVs adhered to dendrites were time-lapse confocal images acquired (16/26 Aβ-EVs, 6/9 ctrl-EVs, $n = 13$ experiments). Confocal analysis showed that Aβ-EVs or ctrl-EVs induced a significant increase in the density of dendritic spines around the contact site (<7 μm from the contact point) from 2 min after adhesion (Fig. 2B and C). The maximal effect was observed 30–40 min after contact (spine density increase: 146.33 ± 9.29% ctrl-EVs; 133.20 ± 13.98% Aβ-EVs; Fig. 2B and C). Almost no impact of EVs (Aβ-EVs or ctrl-EVs) was observed far from the contact site (>60 μm), where the spine density remained unchanged, at any time point (Fig. 2B and D), indicating that EVs act locally.

When we classified dendritic protrusions as mature and immature, based on morphological parameters (spine length, head diameter, neck width), we found that Aβ-EVs significantly increase the

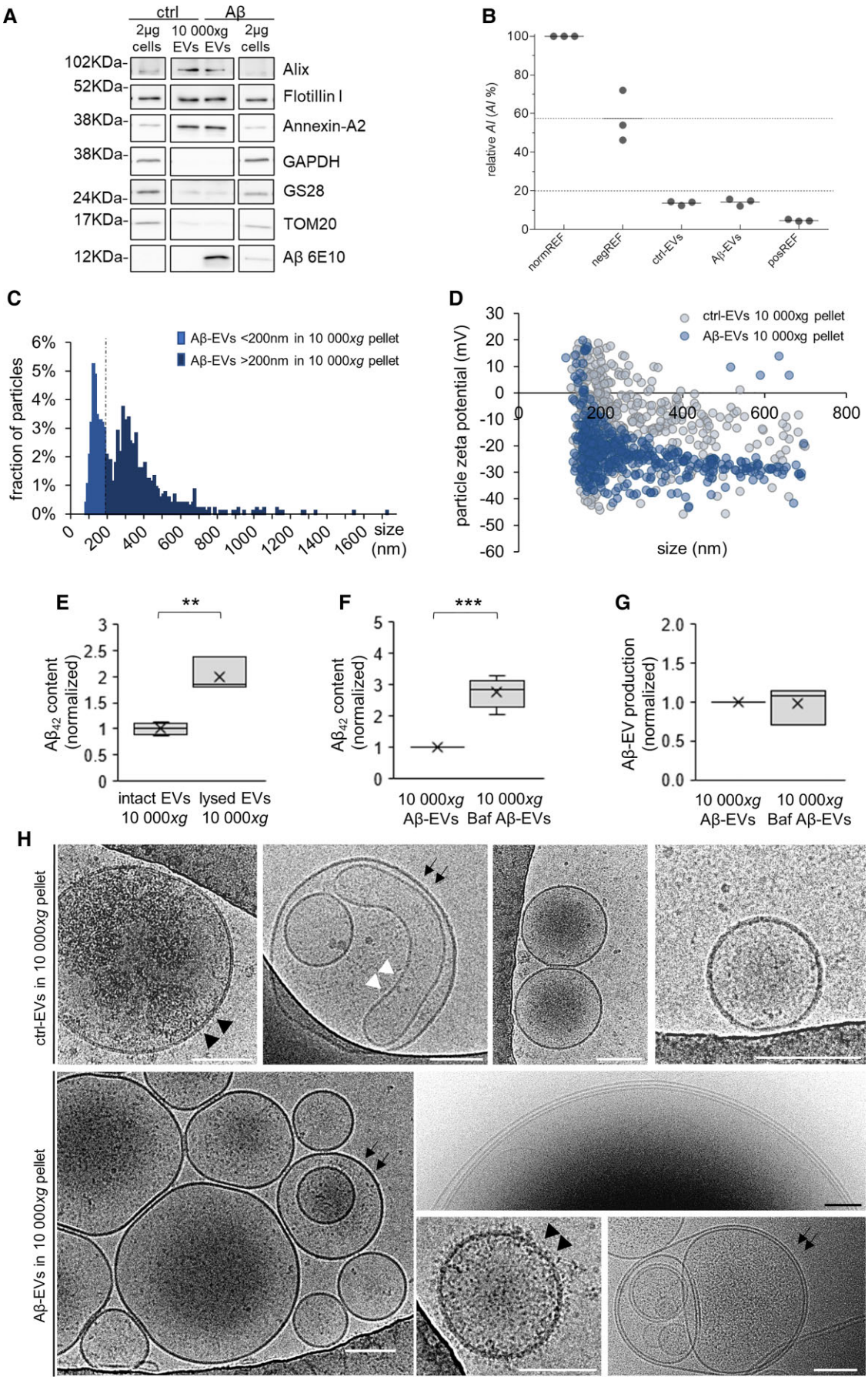

Figure 1 Morphological features and $A\beta_{42}$ content of Aβ-EVs in the 10 000*g* pellet. (**A**) Western blot analysis for the EV markers flotillin I,
(Continued)

number of immature (thin) protrusions at the contact site (Fig. 2B and E), while ctrl-EVs enhanced the number of mature (mushroom, stubby) spines (Fig. 2B and G). No alterations in spine shape were observed far from the contact site (>60 µm; Fig. 2B, F, and H). Consistent with a local EV action, changes in dendritic spine density and morphology were less pronounced when measured along the entire length (~80 µm) of the dendrite in contact with Aβ-EVs or ctrl-EVs 40 min after adhesion (Supplementary Fig. 2A). Interestingly, Aβ-EV-induced spine thinning involved both newly generated (Supplementary Fig. 2B) and pre-existing protrusions (Supplementary Fig. 2C).

By decreasing the spine size, Aβ-EVs might affect synapse stability upon longer exposure. To assess this hypothesis, we next exposed hippocampal neurons to large Aβ-EVs (0.6×10^8 EVs/ml, i.e. 49 pM surface $A\beta_{42}$), ctrl-EVs (0.6×10^8 EVs/ml) or vehicle for 3 h in bulk. Cultures were then fixed and stained for the pre-synaptic active zone protein Bassoon and the post-synaptic marker Shank-2. Analysis of Bassoon and Shank-2 double positive puncta showed a significant decrease in juxtaposed pre- and post-synaptic terminals in Aβ-EV-treated compared to vehicle-treated or ctrl-EV-treated neurons (Fig. 2I and J), revealing that Aβ-EVs impair synaptic stability on a longer timescale. Conversely, ctrl-EVs did not increase the number of juxtaposed pre- and post-synaptic terminals, suggesting that dendritic spines formed shortly after ctrl-EV-neuron contact do not assemble with pre-synaptic boutons to make stable synaptic terminals in the long/medium term.

Next, we asked whether dendritic spine alterations were associated with changes in synaptic plasticity. Neurons were exposed to Aβ-EVs, ctrl-EVs or vehicle for 1 h (0.6×10^8 EVs/ml) as described above. After treatment, EVs were washed out and mEPSCs, corresponding to the spontaneous and random release of neurotransmitter from the pre-synaptic terminal, were measured through single cell whole-cell patch clamp recordings. When synaptic plasticity was evoked using a protocol that chemically induces potentiation through a brief application of glycine (3 min, 200 µM, in Mg^{2+}-free solution),[69] we found that neurons treated with Aβ-EVs lost their capability of undergoing a long-lasting increase in mEPSC frequency compared to vehicle and ctrl-EV treated neurons (Fig. 2K and L). Accordingly, immunofluorescence analysis of puncta positive for the post-synaptic marker PSD-95 and the pre-synaptic marker VGlut-1 before and after chemical LTP[70] revealed that the area of PSD-95 positive and VGlut-1/PSD-95 double positive puncta does not increase in Aβ-EV-treated neurons after plasticity induction, as opposed to vehicle-treated neurons (Supplementary Fig. 3). Collectively, these data indicate that Aβ-EVs selectively affect synaptic plasticity in cultured neurons.

Large Aβ-EVs move along the axons of cultured neurons

Our recent work shows that a fraction of large EVs derived from astrocytes moves at the surface of cultured neurons exploring actin protrusions and use neurites as routes to pass between connected cells.[54] Based on this evidence, we first explored whether EVs of microglial origin may similarly move at the neuron surface. Using optical tweezers, we gently placed single large EV on cell bodies and neurites of developing hippocampal neurons, cultured from 2 to 12 DIV and examined EV–neuron interaction in bright field through live microscopy. While a low percentage of microglial EVs moved on the neuron cell bodies (12.5%, $n = 2/16$), about 53% of EVs displayed extracellular motion along neurites ($n = 19/36$), proving that large microglial EVs can also use neurites to move into the extracellular space. Next, we monitored the dynamics of large Aβ-EVs or ctrl-EVs at the axon surface of fully differentiated neurons (13–17 DIV) for up to 40 min (Fig. 3A). Axons were distinguished from dendrites by their smaller size and the absence of spines on RFP-transfected neurons. A similar percentage of large Aβ-EVs adhered to the axonal surface compared to ctrl-EVs (48% versus 44%; Fig. 3E), ruling out a major involvement of Aβ in the establishment of EV–neuron contact. After adhesion, about 85% of Aβ-EVs displayed net movement from the contact site, surfing on the axon plasma membrane (Fig. 3B, C, F and Supplementary Video 1), while only a few Aβ-EVs (15%) were virtually immobile (EV displacement < EV diameter) or displayed only random Brownian motion (being connected to the axon by a tether) and were considered static (Fig. 3D and F). Notably, Aβ-EVs were more prone to motility compared to ctrl-EVs, as almost twice the number of Aβ-EVs were able to move at the axon surface (85% versus 45%; Fig. 3F). Analysis of EV motion by a custom MATLAB code revealed higher average speed for Aβ-EVs compared to ctrl-EVs (116.56 ± 20.31 nm/s versus 48.20 ± 21.01 nm/s, Fig. 3G), longer pathlength (78.98 ± 14.07 µm/10 min versus 42.72 ± 17.19 µm/10 min, Fig. 3H) and run distance from the contact point (7.55 ± 1.51 µm/10 min versus 4.37 ± 1.65 µm/10 min, Fig. 3I). In addition, visualization of EV trajectories revealed that most Aβ-EVs (~67%) moved in an anterograde (towards the periphery) rather than retrograde (towards the cell body) direction along the axons (number of EVs = 10/15, 11 experiments; Fig. 3J), while most ctrl-EVs exhibited retrograde motion (~60%, number of EVs = 9/15, 7 experiments; Fig. 3J). Next, we asked what percentage of large Aβ-EVs could be internalized inside axons instead of moving anterogradely. We labelled EVs with the fluorescent dye mCLING and analysed by confocal microscopy the localization of mCLING-labelled EVs 1 h after in bulk addition to neurons transfected with membrane-targeted GFP. Confocal analysis revealed that the vast majority of large Aβ-EVs, but also ctrl-EVs, remained outside the axons (97% Aβ-EVs, $n = 101$ EVs; 97% ctrl-EVs, $n = 39$ EVs;

Figure 1 Continued
alix and annexin-A2, the Golgi and mitochondria markers GS28 and TOM20, the cytosolic marker GAPDH and for Aβ (6E10) of EVs in the 10 000*g* pellet from 10×10^6 microglia and relative donor cells (2 µg cell lysate). Normalization to total proteins is shown in Supplementary Fig. 1. (**B**) Analysis of the purity of EV preparations from $A\beta_{42}$-treated microglia and control cells using the CONAN assay; AI% is the relative aggregation index of AuNPs, normREF is a sample of monodispersed AuNPs, negREF (HPLC grade water+AuNPs+PBS solution) is the negative control threshold and posREF is the positive control (PBS solution+AuNPs). (**C**) Size distribution of large Aβ-EVs enriched fraction analysed by TRPS. The fraction of Aβ-EVs of diameter >200 nm represents ~59% of the 10 000*g* pellet. (**D**) Charge measurements of large ctrl-EVs and Aβ-EVs (10 000*g* pellet) by TRPS. Ctrl-EVs display an averaged surface charge of −10.75 mV, while Aβ-EVs −22.57 mV (t-test, $P < 0.001$). (**E**) $A\beta_{42}$ content in intact Aβ-EVs or Aβ-EVs lysed with 0.57% Triton X-100 (10 000*g* pellet), as detected by ELISA. Values are normalized to intact Aβ-EVs (t-test, $P = 0.002$, $n = 3$). (**F**) $A\beta_{42}$ content in large Aβ-EVs enriched fraction (10 000*g* pellet) produced by microglia exposed for 20 h to $A\beta_{42}$ with or without Bafilomycin A1 (Baf) during the last 15 h of treatment, as detected by ELISA in the presence of 0.57% Triton X-100. Values are normalized to the condition without Baf (Mann–Whitney Rank Sum Test, $P < 0.001$, $n = 7$). (**G**) Aβ-EVs in the 10 000*g* pellet from microglia stimulated as in **F**. Values (EV numbers) are normalized to the condition without Baf. Mann–Whitney Rank Sum Test, $P = 0.908$, $n = 3$. (**H**) Representative cryo-electron microscopy micrograph of ctrl- and Aβ-EVs in the 10 000*g* pellet. Arrows point to multilamellar EVs; black arrowheads to EVs with rough surface; white arrowhead to tubular vesicles. Scale bars: 100 nm. Box plots show the median (central line) and mean (X), upper and lower quartile (box limits), maximum and minimum values (whiskers).

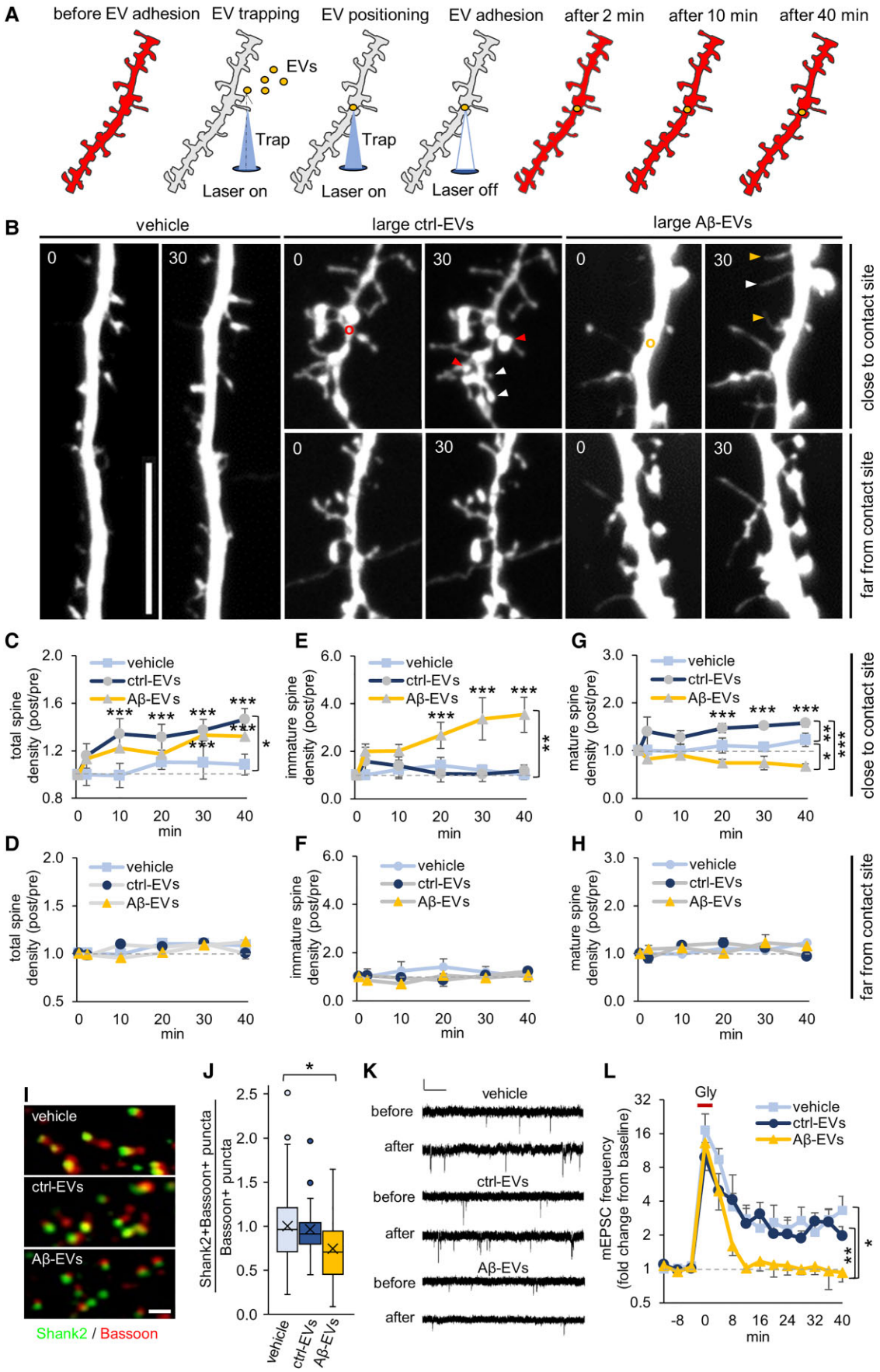

Figure 2 Large Aβ-EVs alter dendritic spine morphology and synaptic plasticity in cultured neurons. (**A**) Schematic representation of EV

(Continued)

Supplementary Fig. 4), in agreement with our previous observation that large EV size is a key factor retaining EVs at the neuron surface.[54] Altogether, these data indicate that Aβ-EVs move extracellularly along axonal projections, with a prevalent anterograde direction, supporting the hypothesis that they may propagate Aβ-mediated synaptic alterations among synaptically connected neurons.

Notably, Aβ-EVs motion was significantly decreased when large EVs were pre-treated with annexin-V (8.4 μg/ml, 30 min), a molecule commonly used to inhibit signalling of large EVs to receiving cells.[71] Annexin-V cloaks phosphatidylserine residues, externalized on the surface of large EVs,[59] and alters EV–cell interaction.[61] Aβ-EVs coated with annexin-V (coated-Aβ-EVs) adhered more efficiently to neurons (from 48% to 73% of adhesion; Fig. 3K), remained outside the axons, as indicated by analysis of mCLING-coated-Aβ-EVs localization in GFP-expressing neurons (coated-Aβ-EVs outside neurons 97%, $n = 63$ EVs) and moved less along the axons of cultured neurons (from 85% to 44% of motion; Fig. 3L). The speed of coated Aβ-EVs still moving at the neuron surface was not significantly affected (73.01 ± 15.66 nm/s for coated-Aβ-EVs compared to 116.56 ± 20.31 nm/s for Aβ-EVs; Fig. 3M).

Large Aβ-EVs propagate LTP impairment in the entorhinal–hippocampal circuit

Encouraged by the finding that large Aβ-EVs impair synaptic plasticity and move along the axons of cultured neurons, we next examined whether Aβ-EVs may induce and spread synaptic dysfunction in the adult mouse brain. First, we extrapolated findings on synaptic plasticity from cell cultures to LTP, a form of synaptic plasticity thought to underlie learning and memory,[72] in the slice preparations, which have an intact neuronal circuitry. In particular, we investigated whether large Aβ-EVs are able to impair LTP in mouse EC slices, a crucial site for memory formation, particularly vulnerable in Alzheimer's disease.[13,26,73] Horizontal sections of entorhinal slices were treated with 1×10^8 Aβ-EVs/ml (equal to 82 pM surface $Aβ_{42}$), ctrl-EVs (1×10^8 EVs/ml), or vehicle for 1 h. LTP was induced by high-frequency stimulation (HFS; 3 trains of 100 pulses at 100 Hz, at 10 s intervals) of EC superficial layer II[64–66] and extracellular field potentials were recorded from the same layer. The study of basal synaptic transmission, measured through analysis of the input/output relationship, did not reveal any difference between slices treated with Aβ-EVs, ctrl-EVs or vehicle (Fig. 4A). LTP was reliably elicited in slices incubated with ctrl-EVs (Fig. 4B). The mean LTP was 131 ± 4 (SEM) % of baseline amplitude 40 min after HFS, similar to vehicle-treated slices. By contrast, LTP was not elicited in Aβ-EV-treated EC slices (Fig. 4B). Note that the concentration of EV surface $Aβ_{42}$ estimated by ELISA (82 pM) is considerably lower than that of oligomeric $Aβ_{42}$ alone, which impairs LTP in EC slices (200 nM in our papers).[65,66] Thus, EVs are capable of enhancing the synaptotoxic effect of Aβ on EC intrinsic circuitry.

Subsequently, we examined whether large Aβ-EVs may spread synaptic dysfunction in the entorhinal-hippocampal circuit. Using EC–hippocampal slices,[65] we measured LTP both in the EC and in its main target region, the ipsilateral DG, 1 h and 24 h after stereotaxic injection of Aβ-EVs or ctrl-EVs (0.25×10^8 EVs, from the large EV-enriched fraction, diluted in 1 μl; 20 nM $Aβ_{42}$) in the EC of adult mice (Fig. 4C). Indeed, considering the speed at which Aβ-EVs move *in vitro* (116.56 nm/s equal to 419.62 μm/h), we reasoned that 24 h was enough time in order to reach the DG moving along the perforant pathway (PP), which is 1.5–3 mm in length.[74] The accuracy of the injection site was checked by injecting PKH26 Red Fluorescent Dye (Merck) in the mouse brain using the same coordinates as for EV injections (AP −3.8 mm, ML ±4.0 mm from Bregma, measured on the skull surface; Supplementary Fig. 5).

Extracellular recordings from the EC superficial layer II revealed a block of LTP 1 h after Aβ-EV injection, whereas a stable LTP was recorded in the contralateral EC injected with ctrl-EVs (Fig. 4D). Extracellular recordings at the synapse between the PP and the DG (PP–DG) showed normal LTP 1 h after Aβ-EV injection following a theta burst simulation (TBS; 10 bursts of 5 pulses at 100 Hz with 250 ms between bursts, as described in Criscuolo *et al.*[64]; Fig. 4E). However, 24 h later, LTP was blocked not only in the EC (Fig. 4D) but also at the PP–DG synapse (Fig. 4E), indicating propagation of LTP impairment between the two connected regions. Similar results have been obtained injecting ∼half-dose of Aβ-EVs (0.11×10^8 in 1 μl; 9 nM $Aβ_{42}$; Supplementary Fig. 6). On the contrary, when we unilaterally injected soluble oligomeric $Aβ_{42}$ (1 μl; 100 nM) in the EC, LTP

Figure 2 Continued

delivery by optical tweezers to RFP-expressing dendrite, preceded and followed by time-lapse imaging of RFP-positive dendritic spines. A *z*-stack of RFP-positive dendrites was first acquired with a spinning disk microscope, then a low amount of EVs was added to the cell medium and one EV was captured (trapped) above the neurons by the infrared laser tweezers and placed in contact with the imaged dendrite (bright field). After 30 s the laser was switched off, EV adhesion was checked and confocal images were collected at the indicated time points. (**B**) Representative confocal images taken before and 30 min after contact of ctrl-EVs (*centre*) or Aβ-EVs (*right*) following the procedure described in **A**, showing dendritic spine changes in proximity (*top*) and far from the EV contact site (*bottom*). Red and orange circles indicate the site of EV contact. White arrows point to newly generated protrusions. Red arrows point to enlarged spines. Orange arrows point to thinned spines. On the *left*, dendritic spine images at 0 and 30 min after vehicle addition. Scale bar: 10 μm. (**C** and **D**) Temporal analysis of dendritic spine density around the contact site (<7 μm, **C**) and far from the contact site (>60 μm, **D**; $n = 6$ dendrites/condition, 12 experiments). Values are normalized to the pre-adhesion condition (two-way repeated measures ANOVA, followed by the Holm–Sidak method; close to the contact site: $P = 0.013$ ctrl-EVs versus vehicle; $P < 0.001$ Aβ-EVs 30 and 40 min versus 0; far from the contact site: $P = 0.937$). (**E**–**H**) Temporal analysis of the density of immature (thin) and mature (mushroom and stubby) dendritic spines around the contact site (**E** and **G**) and far from the contact site (**F** and **H**) after adhesion of Aβ-EVs or ctrl-EVs or in vehicle-treated neurons (immature spines at the contact site: $P < 0.01$ Aβ-EVs versus ctrl-EVs and versus vehicle; $P < 0.001$ Aβ-EVs 20, 30, 40 min versus 0; immature spines far from the contact site: $P = 0.656$; mature spines at the contact site: $P < 0.001$ Aβ-EVs versus ctrl-EVs; $P = 0.015$ Aβ-EVs versus vehicle; $P < 0.01$ ctrl-EVs versus vehicle; $P < 0.001$ ctrl-EVs 20, 30, 40 min versus 0; mature spines far from the contact site, ns). (**I**) Representative images showing Shank-2/Bassoon double-positive puncta in vehicle-treated neurons, neurons exposed to ctrl-EVs or Aβ-EVs. Scale bar: 1 μm. (**J**) The box plot shows the corresponding fraction of juxtaposed pre- and post-synaptic puncta relative to Bassoon positive synaptic puncta (Kruskal–Wallis one-way ANOVA on Ranks, followed by Dunn's method, $P < 0.05$ Aβ-EVs versus vehicle; $n = 3$ experiments). Box plot shows the median (central line) and mean (X), upper and lower quartile (box limits), maximum and minimum values (whiskers). (**K**) Representative traces of mEPSCs recorded from control neurons (vehicle) and neurons exposed to Aβ-EVs or ctrl-EVs for 1 h, before and after induction of synaptic plasticity. Vertical scale bar: 5 pA; horizontal scale bar: 1 s. (**L**) Temporal plot of mEPSC frequency changes showing that glycine (Gly, 200 μM 3 min in 0 Mg^{++}, preceded by 1 min 0 Mg^{++}) induced a long-lasting increase in mEPSC frequency in both vehicle- and ctrl-EV-treated neurons but not in neurons exposed to Aβ-EVs for 1 h (two-way repeated measures ANOVA, followed by the Holm–Sidak method; 2.931 ± 0.808 'vehicle' fold change from baseline, $P = 0.002$; 2.409 ± 0.549 'ctrl-EVs' fold change from baseline, $P = 0.027$; 0.942 ± 0.156 'Aβ-EVs' fold change from baseline, $P = 0.902$; vehicle versus Aβ-EVs, $P = 0.012$; ctrl-EVs versus Aβ-EVs post Gly, $P = 0.009$; vehicle, $n = 6$ cells; ctrl-EVs, $n = 5$; Aβ-EVs, $n = 8$; 7 experiments). Data are expressed as mean ± SEM.

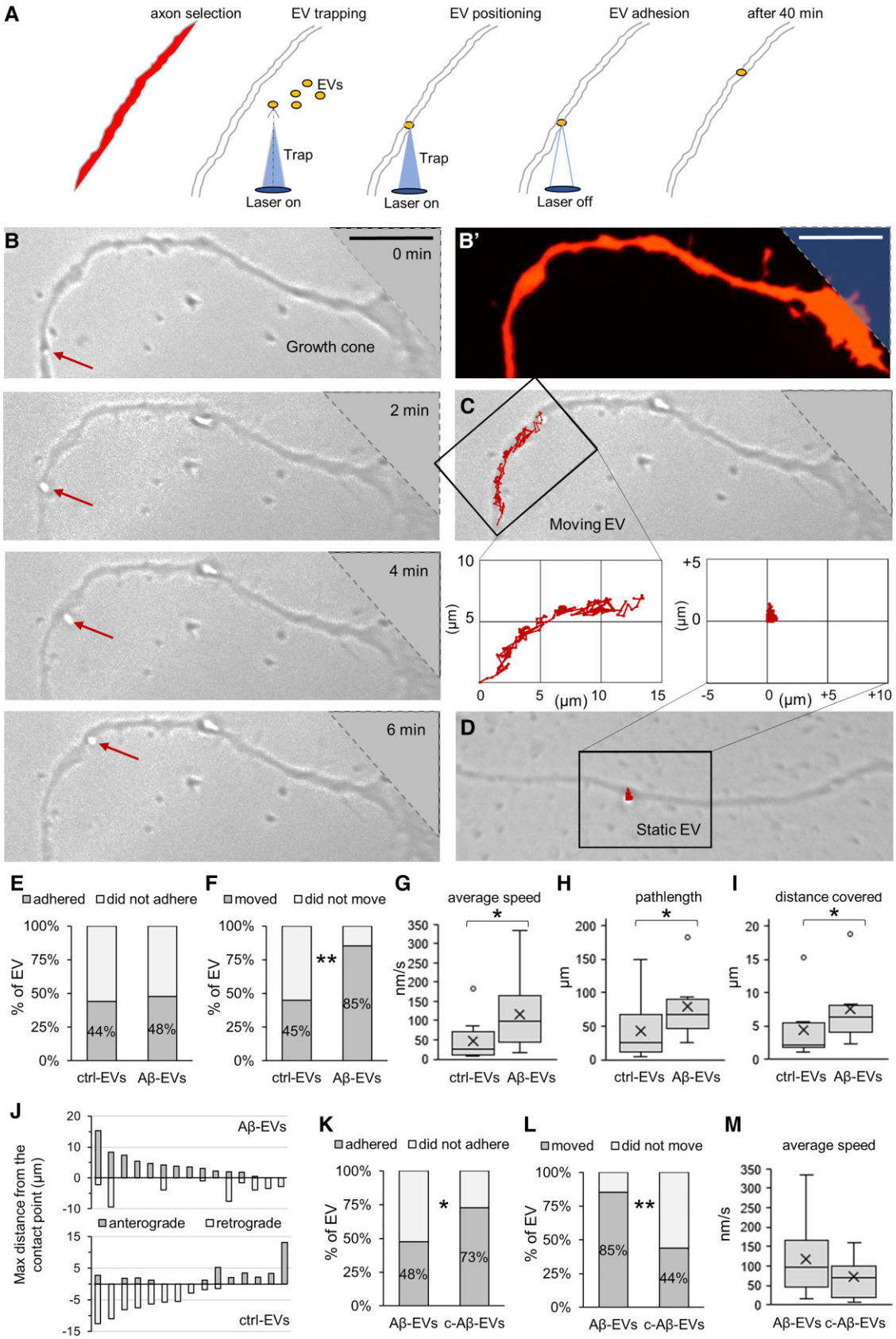

Figure 3 Large Aβ-EV motion at the axon surface. (**A**) Schematic representation of large EV delivery to axons using optical tweezers. Axons were selected based on their morphology after RFP transfection. A single EV was trapped by the laser tweezers in bright field and placed in contact with the axon. The trapping laser was switched off 30 s after contact and EV–axon interaction was monitored in bright field time-lapse for 40 min. (Continued)

was inhibited at this site 1 h after the injection but never in the DG (neither 1 h nor 24 h after injection in the EC; Fig. 4F and G). This indicates that $A\beta_{42}$ alone is not able to propagate among connected regions and requires EVs as vehicle for the transfer. In addition, LTP was completely restored in the EC 24 h after oligomeric $A\beta_{42}$ injection (Fig. 4F), revealing a short-lasting action of free oligomeric $A\beta_{42}$, not associated to EVs. Collectively these findings indicate that, while oligomeric $A\beta_{42}$ alone transiently impairs LTP in the EC, EV-associated Aβ causes a persistent LTP impairment that propagates along the EC–hippocampal circuit.

Next, we aimed at clarifying whether the effect of large Aβ-EVs was dependent on Aβ cargo or other EV component(s) (protein, lipids and miRNAs) sorted in the EVs by Aβ-treated microglia. To this end, microglia were activated with a classical inflammatory stimulus [a cytokine cocktail: 50 ng/ml IL-1β, 20 ng/ml TNF-α, 20 ng/ml INF-γ for 24 h, as in Lombardi *et al.*,[75] which elicits some of the Aβ-induced traits in microglia and EVs (i-EVs) thereof, i.e. similar expression of a set of inflammatory cytokines and miRNAs].[57] Once injected into the EC, i-EVs (0.25×10^8 large EVs diluted in 1 µl, same as Aβ-EVs) were able to impair LTP in the EC either 1 h or 24 h after the injection (Fig. 4H), similarly to Aβ-EVs. However, i-EVs never blocked LTP in the DG (Fig. 4I), revealing that only EVs carrying Aβ propagate LTP defects along the EC–hippocampal connection.

Large Aβ-EVs mainly act on the post-synaptic compartment of the synapse

To characterize the molecular mechanisms underlying Aβ-EV action on the EC–hippocampal circuit, we performed single cell whole-cell patch clamp recordings on pyramidal cells of EC superficial layer II and their main target cells, the granular cells of the DG, 1 h and 24 h after large Aβ-EV injection in the EC of adult mice (0.25×10^8 EVs/1 µl; 20 nM $A\beta_{42}$; Fig. 5A). The contralateral hemisphere was injected with vehicle. We analysed mEPSCs, generally accepted as the post-synaptic response to the spontaneous release of a single quantum of neurotransmitter. In fact, a variation in their frequency is usually related to a change in probability of quantal transmission from the pre-synaptic terminal, whereas a modification in their amplitude is associated with post-synaptic changes. This analysis revealed that Aβ-EVs induce a significant decrease in mEPSC amplitude, with no alteration in their frequency, in pyramidal cells of the EC 1 h after the injection, compared to the cells in the vehicle-injected hemisphere (Fig. 5B and C), mimicking synthetic $A\beta_{42}$ effect.[65] No alteration in mEPSC frequency or amplitude was detected 1 h after ctrl-EV (0.25×10^8 EVs/1 µl) EC injection (frequency 1.96 ± 0.60 Hz, Mann–Whitney Rank Sum Test, $P = 0.841$ versus vehicle; amplitude 9.53 ± 0.81 pA, *t*-test, $P = 0.781$ versus vehicle; $n = 9$, 3 mice). Interestingly, the same decrease in mEPSC amplitude was found in granular cells of the DG 24 h after Aβ-EV injection (Fig. 5D and E). Besides confirming that large Aβ-EVs propagate synaptic dysfunction along the PP, these data revealed that Aβ-EVs resemble synthetic $A\beta_{42}$ action, mostly acting at the post-synaptic site of the synapse.

Large EVs released by microglia exposed to naturally secreted Aβ impair LTP

Data described above and our previous evidence indicate that microglia exposed to micromolar concentration of synthetic $A\beta_{42}$ (mainly in an aggregated form, mimicking extracellular Aβ plaques) generate soluble forms of $A\beta_{42}$, $A\beta_{40}$ and other truncated peptides,[42] which once sorted into large EVs cause and propagate synaptic dysfunction. As at early stages of Alzheimer's disease microglia is exposed to low concentration of oligomeric Aβ form, we found it important to verify whether microglia exposed to nanomolar concentrations of native Aβ forms may also release Aβ-storing EVs, which induce and propagate synaptic dysfunction. To this aim, we incubated primary microglia for 20 h with medium conditioned by CHO7PA2 cells, Chinese hamster ovary cells which stably express the human APP bearing the Val717Phe mutation[56] and release oligomeric Aβ[20] at nanomolar concentrations.[56] Immunostaining with anti-Aβ antibody (6E10) showed that Aβ produced by CHO7PA2 was internalized by microglia (Fig. 6A), albeit in smaller quantities compared to the synthetic peptide.[42] When EVs produced by microglia exposed to CHO7PA2-secreted Aβ (CHO-EVs) were injected in the mouse EC (0.25×10^8 EVs/µl) and LTP was recorded in EC and PP–DG, we observed impaired LTP in the EC 1 h after the injection (Fig. 6B) and at PP–DG synapses 24 h later (Fig. 6C), replicating results obtained with EVs produced by microglia exposed to synthetic $A\beta_{42}$. Thus, large EVs released by microglia exposed to naturally secreted Aβ also cause and propagate LTP deficit in the entorhinal–hippocampal circuit.

Inhibition of large Aβ-EV extracellular motion prevents propagation of synaptic deficits *in vivo*

We finally asked whether reducing EV motility along axonal projections may inhibit the propagation of synaptic defects. To this end, we injected Aβ-EVs coated with annexin-V (c-Aβ-EVs, 0.11×10^8 in 1 µl, 9 nM Aβ; annexin-V, 8.4 µg/ml, 30 min), which move less *in vitro* along axons (Fig. 3L), in the EC of mice. c-Aβ-EVs induced LTP deficit in the EC 1 h after the injection (Fig. 7A), whereas LTP was still present in the DG 24 h after injection (Fig. 7B), indicating that c-Aβ-EVs were not able to propagate synaptic defects. These data provide the first evidence for the involvement of large EV extracellular motion in progression of synaptic dysfunction in Alzheimer's disease.

Figure 3 Continued
(**B**) Sequence of phase contrast images of a large EV moving anterogradely along the axon towards the growth cone. (**B′**) Corresponding fluorescence image of the axon in **B**. The top right blurred area indicates the region of the growth cone outside phase contrast images. (**C**) Trajectory of the EV in B superimposed to the phase contrast image. (**D**) Trajectory of a static EV superimposed to the phase contrast image. (**E**) Percentage of large ctrl-EVs and Aβ-EVs that adhered to axons (chi-square test, $P = 0.768$, $n = 68$ ctrl-EVs, $n = 105$ Aβ-EVs, 33 experiments). (**F**) Percentage of large ctrl-EVs and Aβ-EVs that displayed motility on axons (chi-square, $P = 0.002$, $n = 29$ ctrl-EVs, $n = 34$ Aβ-EVs, 31 experiments). (**G**) Average speed of large Aβ-EVs and ctrl-EVs (Mann–Whitney test, $P = 0.011$, $n = 8$ ctrl-EVs, $n = 18$ Aβ-EVs, 19 experiments). (**H** and **I**) Pathlength (**H**) and maximum distance from the contact point in both directions (**I**) reached by large ctrl-EVs and Aβ-EVs in 10 min (Mann–Whitney, $P = 0.033$, for both; $n = 8$ ctrl-EVs, $n = 13$ Aβ-EVs, 19 experiments). (**J**) Anterograde and retrograde motion of large Aβ-EVs and ctrl-EVs ($n = 15$). (**K**) Percentage of large Aβ-EVs and Aβ-EVs pre-coated with annexin-V (coated Aβ-EVs, c-Aβ-EVs) that adhered to axons (chi-square, $P = 0.014$, $n = 105$ Aβ-EVs, $n = 37$ c-Aβ-EVs, 24 experiments). (**L**) Percentage of large Aβ-EVs and c-Aβ-EVs that displayed motility (chi-square, $P = 0.002$; $n = 34$ Aβ-EVs, $n = 25$ c-Aβ-EVs, 23 experiments). (**M**) Average speed of large Aβ-EVs and c-Aβ-EVs (*t*-test, $P = 0.142$, $n = 18$ Aβ-EVs, $n = 11$ c-Aβ-EVs, 16 experiments). Scale bars: 10 µm. Percentage values are raw percentages over total EV tested. Box plots show the median (central line) and mean (X), upper and lower quartile (box limits), maximum and minimum values (whiskers).

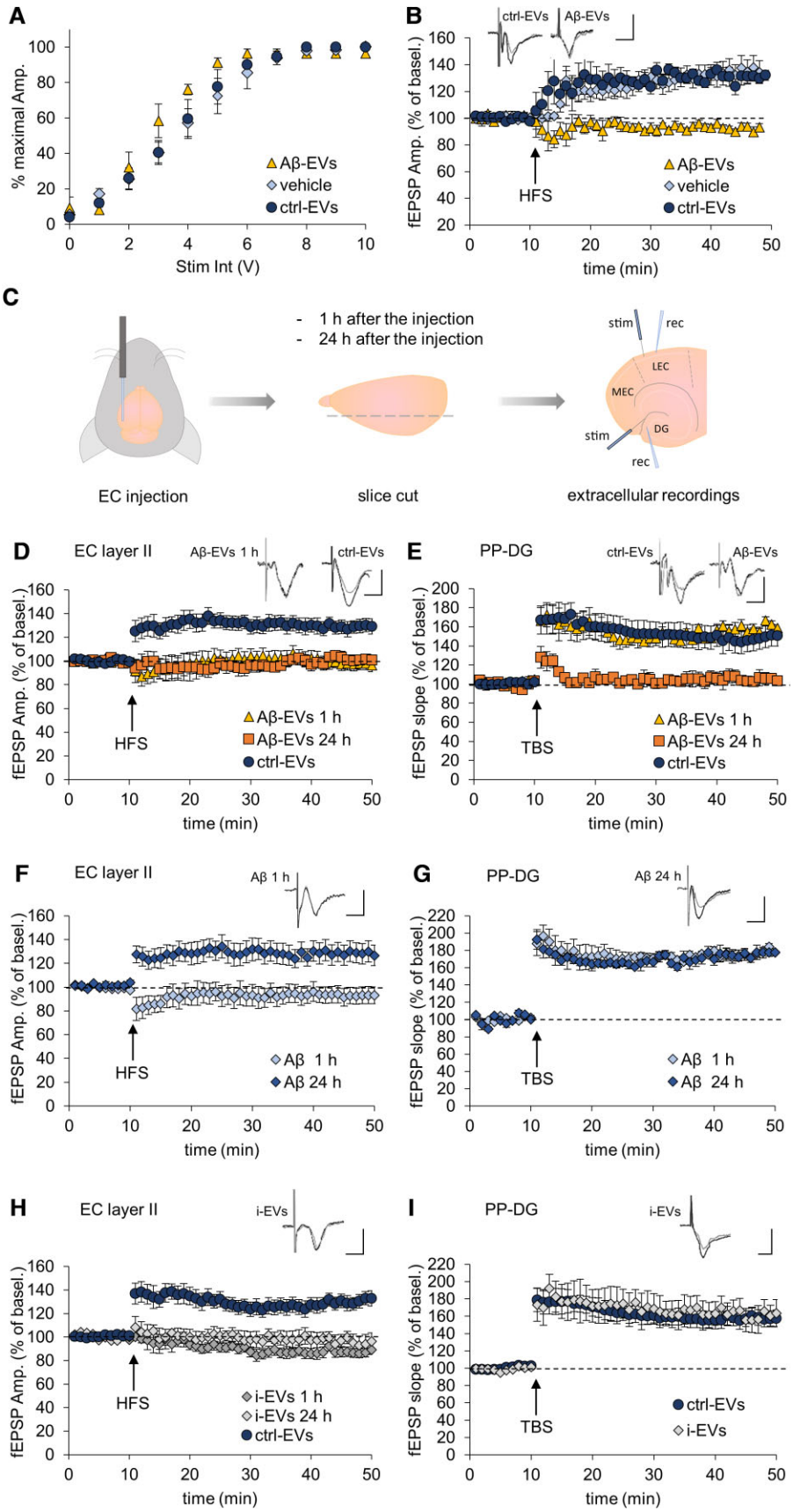

Figure 4 Large Aβ-EVs propagate LTP impairment in the EC–DG circuit. (**A**) Input–output curves showing the relative amplitude (% maximal Ampl.) as a function of stimulus intensity [Stim. Int., measured in volts (V)] in vehicle-treated slices and slices exposed to 1×10^8/ml Aβ-EVs, ctrl-EVs (Continued)

Discussion

Alzheimer's disease is a neurodegenerative disorder that involves increasingly larger areas of the brain over time, and has been proposed to spread along the neuronal network through defined topographical patterns. Disruption of synaptic functionality and abnormal microglial function have been recently identified as early mechanisms in the disease, preceding aggregate formation and neuronal damage in vulnerable brain regions. However, we still lack a full understanding of how synaptic dysfunction originates, propagates and is linked to microglial activation in the affected brain. There is an urgent need to address these questions in order to design treatments to delay Alzheimer's disease onset and/or progression, as current drugs treat symptoms, temporarily helping memory and thinking problems, but do not interrupt the disease process.[76,77]

In this study, we unveil a novel mechanism through which microglia contribute to the onset and propagation of early synaptic dysfunction along the entorhinal–hippocampal circuit, a brain region primarily affected in Alzheimer's disease. We show that large EVs, released by primary microglia that have taken up $A\beta_{42}$, locally affect dendritic spine size in cultured neurons, impair synaptic plasticity in culture and brain slices and spread LTP impairment along the entorhinal–hippocampal circuitry.

Amyloid-β exposed on EV surface accounts for synaptic dysfunction

Aβ-EV-mediated synaptic alterations are due to their Aβ cargo, as only EVs carrying the peptide (synthetic or naturally produced by cells) decrease dendritic spine size and impair synaptic plasticity *in vitro* and *in vivo* (EC). Aβ-EV action perfectly mimics that of soluble oligomeric $A\beta_{42}$, which impairs LTP in EC[66] and DG[78] brain slices, acting mainly on the post-synaptic site of the synapse. Specifically, patch clamp recordings from EC pyramidal cells indicate that Aβ-EVs reduce mEPSC amplitude without affecting their frequency, as does $A\beta_{42}$.[65] Moreover, Aβ-EVs shift the balance of dendritic spines towards immature structures in cultured neurons, similarly to oligomeric $A\beta_{42}$,[79] and in agreement with the findings obtained in early stage Alzheimer's disease transgenic mice.[64]

The analogy between the action of free and EV-associated Aβ suggests that the peptide is exposed on EV surface, as previously argued.[43,50] This would also explain the very rapid conversion of dendritic protrusions to immature spines, already detectable 2 min after contact with one single large Aβ-EV.

Consistent with Aβ externalization on large EVs, we here show that (i) $A\beta_{42}$ is detectable by ELISA in large EVs in the absence of any detergent; and (ii) large EVs carrying Aβ, that is enriched in negatively charged residues,[67] exhibit a negative shift in the surface charge with respect to ctrl-EVs, as indicated by TRPS analysis. Importantly, being exposed on the EV surface, Aβ can spread post-synaptic changes through interactors present on the neuron surface without the need of being transferred to the neuron cytoplasm (Fig. 8). This would explain why Aβ-induced synaptic dysfunction largely precedes the appearance of Aβ deposit in Alzheimer's disease affected brain.

Several molecules expressed on the neuron membrane are listed as Aβ interactors and may mediate synaptic deficits induced by surface Aβ.[83–86] Some of these molecules [i.e. α7-nicotinic acetylcholine receptor (α7-nAhR), Ephrin B2 (EphB2), receptor for the advanced glycation end products (RAGE) and cellular prion protein (PrP^C)] act inside dynamic signalling platforms (or signalosomes) located on the post-synaptic membrane of neurons, and signal through the *N*-methyl-D-aspartate receptor (NMDAR), therefore possibly mediating the post-synaptic effects of Aβ-EVs.[84] Their involvement in synaptic dysfunction will need further investigation.

Other component(s) of Aβ-EVs may contribute to synaptic alterations besides Aβ. Accordingly, we show that EVs produced by classical inflammatory microglia (i-EVs), devoid of Aβ,[57,75] are still capable of blocking LTP in the EC, despite not propagating synaptic dysfunction to the DG. In line with this finding, the inflammatory

Figure 4 Continued
or vehicle for 1 h. (**B**) LTP field potential recordings in slices incubated with Aβ-EVs (same amount as in **A**, yellow triangles), ctrl-EVs (dark blue circles) or vehicle alone with no EVs (light blue diamonds). LTP was reliably elicited in slices incubated with ctrl-EVs [two-way repeated measures ANOVA, followed by the Holm–Sidak method, ctrl-EVs 131 ± 4% of baseline amplitude 40 min after HFS ($n = 7$ slices, 4 mice); vehicle 134 ± 7% ($n = 6$ slices, 4 mice); $P = 0.473$ ctrl-EVs versus vehicle], while was not elicited in Aβ-EVs treated EC slices (93 ± 3% of baseline after HFS, $P = 0.154$ versus baseline; $P < 0.001$ versus vehicle and ctrl-EVs; $n = 6$ slices; 4 mice). (**C**) Experimental protocol for LTP measurements in EC–DG slices after large EVs or $A\beta_{42}$ injection. Large Aβ-EVs, ctrl-EVs or i-EVs (0.25×10^8 EVs/μl, 1 μl), $A\beta_{42}$ (1 μl, 100 nM) or vehicle were injected into the mouse lateral EC. Mice were sacrificed 1 h and 24 h after the injection and horizontal slices containing both the EC and the hippocampus have been cut. LTP was recorded from the EC superficial layer II (stimulus and recording pipette in this layer) and at the synapse between the PP (stimulus) and the DG (recording). (**D** and **E**) LTP plots from the EC superficial layer II (**D**) and the PP–DG synapse (**E**) in cortico-hippocampal slices after injection of large Aβ-EVs in the lateral EC or large ctrl-EVs in the contralateral EC. Field recordings in EC superficial layer II revealed suppression of LTP 1 h after the injection of Aβ-EVs in the ipsilateral EC (**D**, yellow triangles), while a stable LTP was recorded in the contralateral EC injected with ctrl-EVs (**D**, dark blue circles; ctrl-EVs 129 ± 6% *versus* Aβ-EVs 99 ± 5%, $P < 0.001$, $n = 8$ slices, 4 mice each). Twenty-four hours after the injection of Aβ-EVs, LTP was still impaired in EC (**D**, orange squares; Aβ-EVs 101 ± 2%, $P < 0.001$ versus ctrl EVs, $n = 7$ slices, 4 mice). In field recordings from the DG after PP stimulation (**E**), LTP was normal 1 h after the injection of Aβ-EVs in the EC (**E**, yellow triangles) and comparable to that obtained in the contralateral hippocampus injected in the EC with ctrl-EVs (**E**, dark blue circles; Aβ-EVs 159 ± 5% versus ctrl-EVs 147 ± 12%, $P = 0.195$, $n = 8$ slices, 4 mice each). In contrast, LTP was blocked 24 h after Aβ-EV injection in the ipsilateral EC (**E**, orange squares; Aβ-EVs 105 ± 8% $P < 0.001$ versus ctrl EVs and Aβ-EVs at 1 h, $n = 7$ slices, 4 mice). (**F** and **G**) Effect of the stereotaxic injection of oligomeric $A\beta_{42}$ in EC on LTP expression in cortico-hippocampal slices. Field recordings in EC revealed that LTP expression is affected 1 h after the injection of $A\beta_{42}$ in the EC (**F**, light blue diamonds; 93 ± 7%, $P = 0.187$ versus baseline, $n = 7$ slices, 4 mice) but it recovers 24 h after $A\beta_{42}$ injection (**F**, dark blue diamonds). Slice recordings from the DG after PP stimulation revealed that hippocampal LTP is normally expressed 1 h after the injection of $A\beta_{42}$ in the EC (**G**, light blue diamonds; 176 ± 4%, $n = 7$ slices, 4 mice) and comparable to that obtained in hippocampal slices 24 h after the injection of $A\beta_{42}$ in the EC (**G**, dark blue diamonds; 176 ± 2%, $P = 0.039$ versus 1 h, $n = 7$ slices, 4 mice). (**H** and **I**) Effect of the stereotaxic injection of i-EVs in the EC on LTP expression in EC–hippocampal slices. Field recordings in EC revealed that LTP expression is affected already 1 h after i-EV injection (**H**, dark grey diamonds; i-EVs 87 ± 4% of baseline amplitude after HFS versus ctrl-EVs 130 ± 6%, $P < 0.001$, $n = 8$ slices, 4 mice each) and remained impaired 24 h after (**H**, light grey diamonds; 96 ± 6% of baseline amplitude, $n = 6$ slices, 4 mice; $P < 0.001$ versus ctrl-EVs and $P = 0.120$ versus i-EVs at 1 h). Hippocampal LTP was normally expressed 24 h after the injection of i-EVs in the EC (**I**, light grey diamonds) and comparable to that obtained in hippocampal slices after the injection of ctrl-EVs in the EC (**I**, dark blue circles; mean LTP was 157 ± 11% of baseline fEPSP slope, $P = 0.469$ versus ctrl-EVs 159 ± 9%, $n = 7$ slices, 4 mice each). *Inserts* show representative traces of field potential. Vertical scale bar: 0.5 mV; Horizontal scale bar: 5 ms. Values are mean ± SEM.

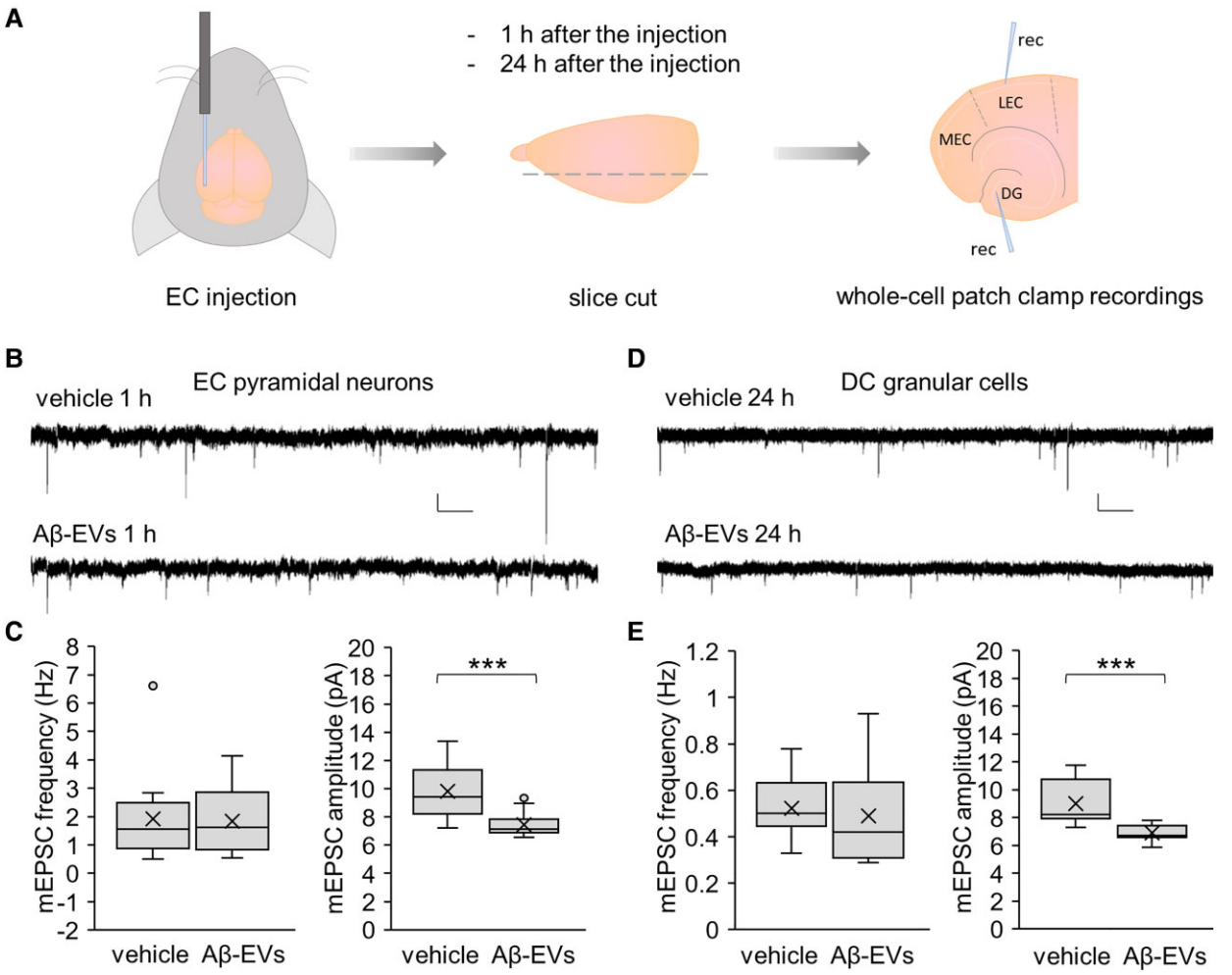

Figure 5 Aβ-EVs decrease mEPSC amplitude without affecting their frequency. (**A**) Experimental protocol for whole-cell patch-clamp recordings in EC–DG slices after Aβ-EV (0.25×10^8 EVs/μl, 1 μl) or vehicle injection. Recording electrodes are shown. (**B** and **C**) Representative traces of mEPSCs recorded from pyramidal cells of EC superficial layer II 1 h after injection of Aβ-EVs or vehicle in the EC (**B**) and corresponding plots of mEPSC frequency and amplitude (**C**; mEPSC frequency, *t*-test, $P = 0.900$; mEPSC amplitude, Mann–Whitney rank sum test, $P \leq 0.001$; vehicle, $n = 13$ cells; Aβ-EVs, $n = 13$ cells; 7 mice each). (**D** and **E**) Representative traces of mEPSCs recorded from granular cells of the DG 24 h after injection of Aβ-EVs or vehicle in the EC (**D**). The plots show corresponding mEPSC frequency and amplitude (**E**; mEPSC frequency, *t*-test, $P = 0.655$; mEPSC amplitude, *t*-test, $P \leq 0.001$; vehicle, $n = 12$ cells; Aβ-EVs, $n = 13$ cells; 6 mice each). Vertical scale bar: 5 pA; Horizontal scale bar: 1 s. Box plots show the median (central line) and mean (X) values, upper and lower quartile (box limits), maximum and minimum values (whiskers).

interferon pathway has been recently shown to possess a potent but incomplete capacity to drive a neurodegenerative phenotype in microglia and synaptic pathology in the mouse brain.[87] Further experiments are needed to identify the inflammatory molecules of i-EVs causing LTP impairment and to define their mode of action.

EVs are essential vehicles for the propagation of synaptic dysfunction

A key strength of our study is the demonstration that microglial EVs are essential vehicles for the spreading of Aβ-dependent synaptic dysfunction. Indeed, while free oligomeric $A\beta_{42}$ is unable to perturb synaptic functionality far from the injection site, packaging into EVs makes Aβ able to spread synaptic plasticity defects along the EC–DG circuitry. Furthermore, packaging into EVs makes Aβ effective at lower concentration compared to free soluble oligomeric $A\beta_{42}$ (9 nM active concentration of EV-associated $A\beta_{42}$ versus 200 nM of free $A\beta_{42}$). This is in line with previous evidence showing that (i) natural lipids shift the equilibrium between insoluble and soluble Aβ toward toxic soluble species[88,89]; (ii) the lipidic EV environment favours the acquisition of synaptotoxic Aβ conformations.[42] Similar roles for EVs have been recently reported in tau pathology.[44,90]

Notably, the action of large EVs produced by microglia exposed to high concentrations of synthetic $A\beta_{42}$ have been validated with EVs derived from microglia exposed to oligomeric Aβ forms released by CHO7PA2 cells at nanomolar concentrations, in a setting which better mimics microglia activation at early Alzheimer's disease stages. However, whether large EVs produced endogenously by microglia may spread synaptic dysfunction in a model of Alzheimer's disease, e.g. mice selectively overexpressing APP/Aβ in the EC,[13] remains unclear. Selective tools to manipulate endogenous production of large EVs are needed to overcome this limitation of our study and to analyse the role of large microglial EVs carrying Aβ in a more physiological context. It should be noted, however, that large EVs carrying Aβ species are present in the CSF of Alzheimer's disease patients[42] and their production

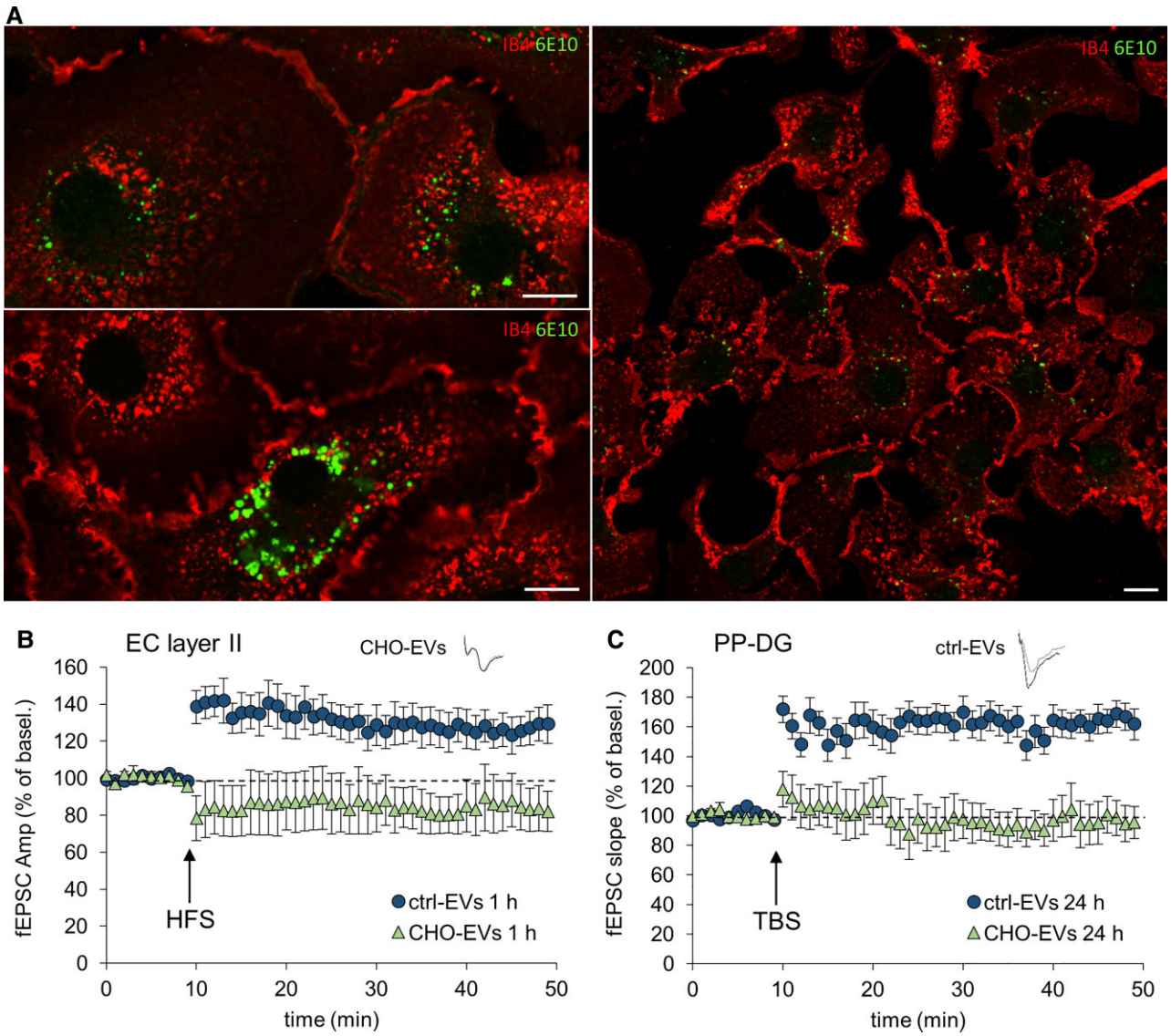

Figure 6 CHO-EVs propagate LTP impairment in the EC–DG circuit. (**A**) Living mouse microglia were exposed to CHO7PA2 cell supernatant containing nanomolar concentrations of Aβ for 20 h and stained with IB4-Alexa568 to label the cell surface before being fixed and counterstained with anti-Aβ antibody 6E10. Scale bar: 10 µm. (**B** and **C**) Effect on LTP expression of the stereotaxic injection in the EC of EVs released by microglia exposed for 20 h to CHO7PA2 cell supernatant (CHO-EVs, 0.25×10^8 EVs/µl, 1 µl), compared to the same amount of ctrl-EVs. LTP plots are relative to recordings from EC and PP–DG, 1 h and 24 h after the injection, respectively (two-way repeated measures ANOVA, followed by the Holm–Sidak method, 1 h EC: 85.48 ± 13.09%, $P = 0.234$ versus baseline; $P = 0.023$ versus ctrl-EVs; $n = 4$ slices CHO-EVs; $n = 6$ slices ctrl-EVs; 24 h PP–DG: 97.29 ± 10.86%, $P = 0.802$ versus baseline; $P < 0.01$ versus ctrl-EVs; $n = 4$ slices CHO-EVs; $n = 6$ slices ctrl-EVs). Vertical scale bar: 0.5 mV; horizontal scale bar: 5 ms. Values are mean ± SEM.

from microglia/macrophages correlates with early brain damage in prodromal Alzheimer's disease,[42,53] thus suggesting the involvement of endogenously produced large microglial EVs in Alzheimer's initiation. In addition, inhibition of EV biogenesis by a brain permeant antagonist of the ATP receptor P2X7 recently revealed an amelioration of disease propagation in a tauopathy mouse model.[46] Despite the fact that the antagonist does not selectively block EV biogenesis in microglia, this study clearly supports a role for EVs endogenously produced in the brain upon ATP stimulation in disease progression.

Whether large EVs of other cell origin (e.g. neurons or astrocytes) can induce similar synaptic dysfunction in the entorhinal–hippocampal circuit is an interesting question, worth addressing in future experiments. Many studies have revealed a role for small-EVs released by neurons or astrocytes as carriers of Alzheimer-related misfolded proteins,[51,80,81,91–94] but their impact on synaptic plasticity has never been explored.

EV motion at the axon surface is involved in the propagation of synaptic dysfunction

Our work indicates a novel extracellular route by which large Aβ-EVs move in the brain parenchyma, spreading synaptic dysfunction. Previous evidence shows that small EVs storing Aβ, isolated from Alzheimer's disease brain, can be internalized by cultured neurons and intracellularly transferred between neurons through axonal projections, spreading neurotoxicity.[80,81] Our study goes well beyond these works by showing that: (i) large Aβ-EVs,

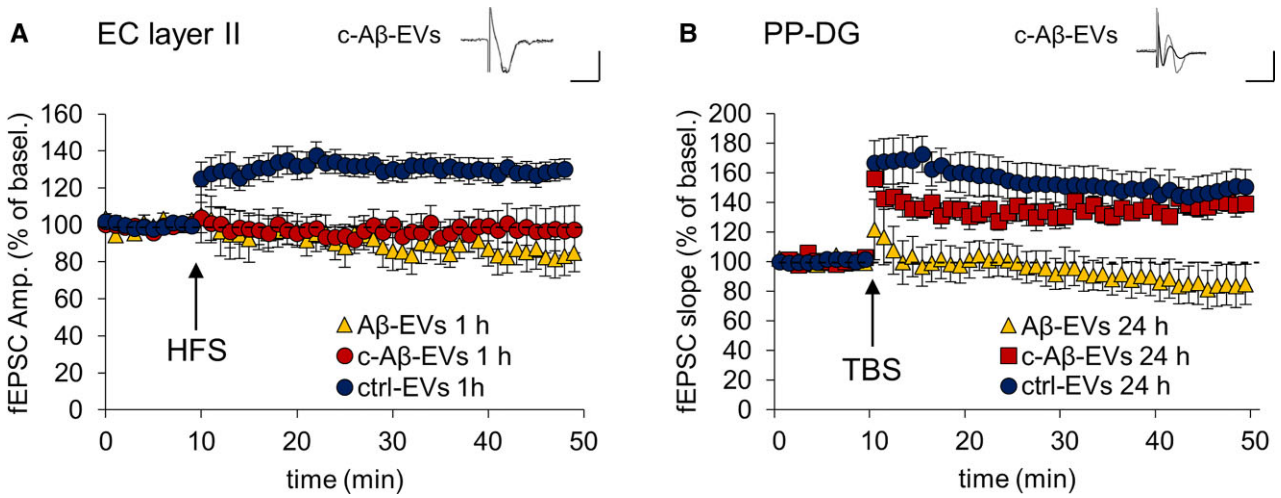

Figure 7 Aβ-EVs coated with annexin-V do not propagate LTP impairment in the EC–DG circuit. (**A** and **B**) Effect of the stereotaxic injection of Aβ-EVs (0.11×10^8 EVs/μl, 1 μl) or coated Aβ-EVs (c-Aβ-EVs; 0.11×10^8 EVs/μl, 1 μl) in the EC on LTP expression in EC and PP–DG, 1 h and 24 h after the injection, respectively. c-Aβ-EVs impaired LTP in EC 1 h after the injection (**A**) (two-way repeated measures ANOVA, followed by the Holm–Sidak method, 97.95 ± 11.19%, $P = 0.820$ versus baseline; $P = 0.152$ versus Aβ-EVs; $n = 8$ slices ctrl-EVs; $n = 6$ slices Aβ-EVs; $n = 7$ slices c-Aβ-EVs; four mice), while allowing its expression in the DG 24 h later (**B**) (137.80 ± 5.64%, $P = 0.008$ versus baseline; $P < 0.001$ versus Aβ-EVs; $n = 8$ slices ctrl-EVs; $n = 8$ slices Aβ-EVs; $n = 6$ slices c-Aβ-EVs; 5 mice). Inserts show a representative trace of field potential. Vertical scale bar: 0.5 mV; horizontal scale bar: 5 ms. Values are mean ± SEM.

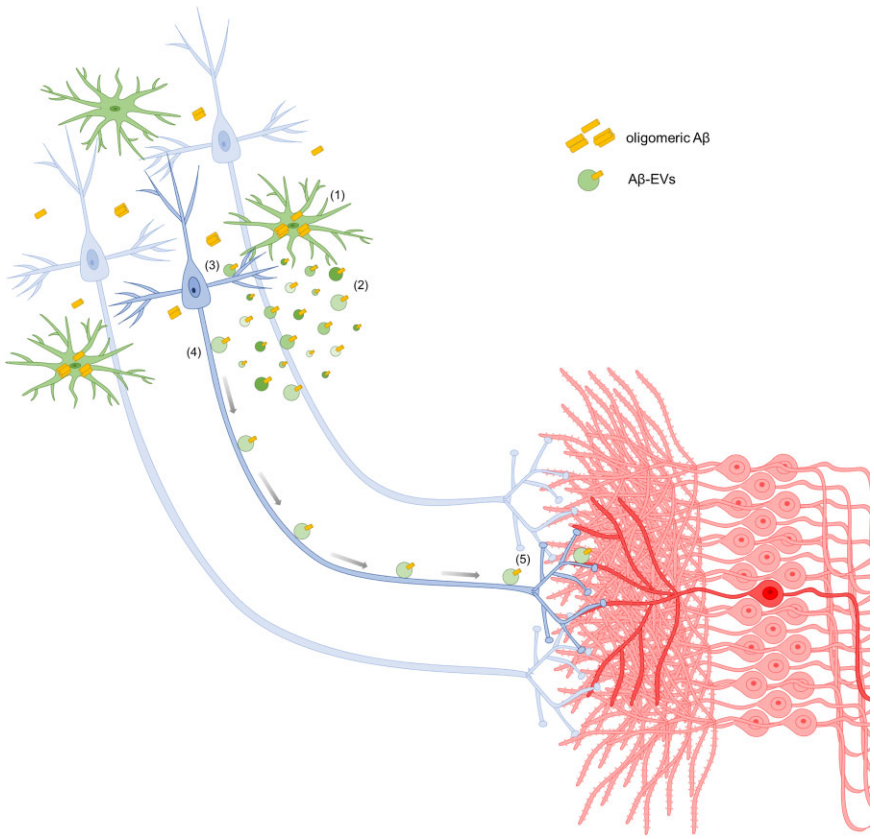

Figure 8 Model for synaptic dysfunction propagation mediated by large Aβ-EVs in Alzheimer's disease. We propose the following model to explain Aβ-EV implication in the onset and propagation of synaptic dysfunction. In the early stages of Alzheimer's disease, Aβ starts to accumulate in specific areas of the brain, where it is internalized by microglia (1) and re-secreted in toxic form in association with EVs (2): the higher the Aβ cell load, the higher the Aβ content (as indicated by Bafilomycin experiments showed in this paper). Aβ-EVs induce synaptic alterations at the site of adhesion (3) and, by moving along axonal projection (4), can reach connected neurons (5). While small EVs are internalized by neurons and travel inside neuronal axons to trans-synaptically transfer their cargo (so far reported for small EVs released by primary neurons or isolated from Alzheimer patients' brains),[80–82] large EVs, likely too big to be transported intracellularly, move at the axonal surface towards synaptically connected cells.

which might not be transported intracellularly without impairing vesicle trafficking, move *in vitro* at the axon surface; (ii) annexin-V coating is a valid treatment to inhibit extracellular EV motion. Annexin-V, bound to phosphatidylserine residues on the EV surface, can link the EV to tether molecule(s) expressed by recipient cells,[95] thus stabilizing EV–neuron contact with axons, inside which large EVs cannot be internalized (this study and D'Arrigo *et al.*[54]), and hampering extracellular EV motion; and (iii) Aβ-EVs injected in the EC impair LTP in both the EC and the DG, while more static Aβ-EVs (annexin-V coated) inhibit LTP only in the EC and cannot propagate LTP impairment to the DG.

Collectively these findings implicate extracellular motion of large Aβ-EVs in the propagation of synaptic dysfunction in the entorhinal–hippocampal circuit. However, due to current limitation of EV imaging in the mouse brain,[96] we do not provide direct evidence for extracellular Aβ-EV motion *in vivo*. Neither can we exclude the possible contribution of small EVs to synaptic alterations, given that small EVs are present in the large EV-enriched fraction injected into the mouse cortex. Thus, we cannot rule out that delayed LTP impairment in the DG might be secondary to some alterations induced by Aβ-EVs on EC layer II cells and that such changes may be inhibited by annexin-V coating similarly to Aβ-EV motion. In future studies, translucent zebrafish embryos, which allow tracking of EVs at single-vesicle level, may help to overcome this limitation of our work.

Exploring EV–neuron interaction dynamics

The employment of optical tweezer technology combined with time-lapse imaging has been fundamental to study the effects of single EV on the synapse and to show for the first time that one single EV (single ctrl- and Aβ-EV tested) is sufficient to elicit a detectable effect (dendritic spine alteration) in a recipient cell. Optical manipulation experiments started from the observation, during live imaging in cultures, that EVs can randomly attach not only to the soma but also to the processes of neurons,[57] suggesting that this technique allows the monitoring of a physiological EV–neuron interaction, which is difficult to be otherwise imaged. Using this approach, we recently showed that astrocytic EVs move at the neuron surface with a speed similar to that previously reported for small exosomes, which surf along filopodia to enter cells at endocytic hot spots.[97] In addition, we showed that the motion of most astrocyte-derived EVs at the neuron surface is driven by the interaction of the prion protein (PrP) on EVs with its neuronal receptor(s), which elicit(s) EV motion by linking EVs to a dynamic actin cytoskeleton.[54] Neuronal receptors of vesicular PrP include PrP itself, which can undergo homophilic interaction with PrP molecule in trans,[98,99] eliciting EV–neuron contact. Importantly, Aβ on the vesicular surface can also interact with neuronal PrP, and this might explain why Aβ-EVs move more efficiently compared to ctrl-EVs. However, other surface molecules of Aβ-EVs may control EV docking and extracellular motion, e.g. intercellular adhesion molecules (ICAMs) which bind to integrins, integrins themselves, lectins (e.g. galectins 1, 3) that interact with proteoglycans.[95,100,101] All these molecules, along with PrP, also stimulate neurite outgrowth[102] and may therefore be responsible for the ability of microglial EVs (both ctrl-EVs and Aβ-EVs) to promote formation of actin protrusions, including spine–head filopodia,[103] at EV–neuron contact sites, mimicking the ability of parental microglia to induce spine formation at microglia–synapse contact sites.[103] With respect to the prevalent anterograde direction of Aβ-EV motion, we speculate that surface proteins unique of Aβ-EVs may drive the interaction of Aβ-EVs with neuronal receptors characterized by prevalent anterograde motion.

To conclude, a new model emerges from our study, which points to a central role for large microglial EVs, carrying surface Aβ, in the onset and propagation of early synaptic dysfunction throughout Alzheimer-specific topographical patterns (Fig. 8). Despite being less studied compared to small EVs (exosomes), large EVs are functionally not less relevant and may be the target of novel strategies to counteract Alzheimer's disease onset and progression.

Acknowledgements

We thank Arianna Chesi for helping in some experiments, Dr Paolo Swuec (University of Milan, Milan, Italy) for cryo-electron microscopy analysis of EVs and Dr Dan Cojoc (CNR Institute of Materials, Trieste, Italy) for help in setting the optical tweezer system.

Funding

This work was supported by American National Institutes of Health (NIH) 1R56AG056108-01 to O.A. and C.V. by Alzheimer's Association Research Fellowship (AARF) 2018-AARF-588984 to I.P., and by Italian Multiple Sclerosis Foundation (FISM) cod. 2018/R/22 and financed or co-financed with the '5 per mille' public funding to C.V. M.G. was supported by a FISM senior research fellowship (cod. 2016/B/2) and financed or co-financed with the '5 per mille' public funding.

Competing interests

O.A. is a founder of Neurokine Therapeutics. O.A. has received research funding from Appia Pharmaceuticals LLC. M.G., I.P., G.D.A., P.J., C.F., G.R., E.B., R.Z., F.T., A.R., N.O. and C.V. report no competing interests.

Supplementary material

Supplementary material is available at *Brain* online.

References

1. Selkoe DJ. Normal and abnormal biology of the beta-amyloid precursor protein. *Annu Rev Neurosci*. 1994;17:489–517.
2. Salter MW, Stevens B. Microglia emerge as central players in brain disease. *Nat Med*. 2017;23(9):1018–1027.
3. Braak H, Braak E. Neuropathological staging of Alzheimer-related changes. *Acta Neuropathol*. 1991;82(4):239–259.
4. Thal DR, Rüb U, Orantes M, Braak H. Phases of Aβ-deposition in the human brain and its relevance for the development of AD. *Neurology*. 2002;58(12):1791–1800.
5. Braak H, Alafuzoff I, Arzberger T, Kretzschmar H, Del Tredici K. Staging of Alzheimer disease-associated neurofibrillary pathology using paraffin sections and immunocytochemistry. *Acta Neuropathol*. 2006;112(4):389–404.
6. Buckner RL, Snyder AZ, Shannon BJ, *et al*. Molecular, structural, and functional characterization of Alzheimer's disease: Evidence for a relationship between default activity, amyloid, and memory. *J Neurosci*. 2005;25(34):7709–7717.
7. Huijbers W, Mormino EC, Wigman SE, *et al*. Amyloid deposition is linked to aberrant entorhinal activity among cognitively normal older adults. *J Neurosci*. 2014;34(15):5200–5210.

8. Sepulcre J, Schultz AP, Sabuncu M, *et al*. *In vivo* tau, amyloid, and gray matter profiles in the aging brain. *J Neurosci*. 2016;36-(28):7364–7374.
9. Selkoe DJ. Alzheimer's disease is a synaptic failure. *Science*. 2002;298(5594):789–791.
10. Selkoe DJ, Hardy J. The amyloid hypothesis of Alzheimer's disease at 25 years. *EMBO Mol Med*. 2016;8(6):595–608.
11. Masliah E, Mallory M, Alford M, *et al*. Altered expression of synaptic proteins occurs early during progression of Alzheimer's disease. *Neurology*. 2001;56(1):127–129.
12. Terry RD, Masliah E, Salmon DP, *et al*. Physical basis of cognitive alterations in Alzheimer's disease: Synapse loss is the major correlate of cognitive impairment. *Ann Neurol*. 1991;30(4): 572–580.
13. Harris JA, Devidze N, Verret L, *et al*. Transsynaptic progression of amyloid-beta-induced neuronal dysfunction within the entorhinal–hippocampal network. *Neuron*. 2010;68(3):428–441.
14. DeKosky ST, Scheff SW. Synapse loss in frontal cortex biopsies in Alzheimer's disease: Correlation with cognitive severity. *Ann Neurol*. 1990;27(5):457–464.
15. Lambert MP, Barlow AK, Chromy BA, *et al*. Diffusible, nonfibrillar ligands derived from $A\beta_{1\text{-}42}$ are potent central nervous system neurotoxins. *Proc Natl Acad Sci USA*. 1998;95(11):6448–6453.
16. Shankar GM, Li S, Mehta TH, *et al*. Amyloid-beta protein dimers isolated directly from Alzheimer's brains impair synaptic plasticity and memory. *Nat Med*. 2008;14(8):837–842.
17. Masliah E. Mechanisms of synaptic dysfunction in Alzheimer's disease. *Histol Histopathol*. 1995;10(2):509–519.
18. Oddo S, Caccamo A, Shepherd JD, *et al*. Triple-transgenic model of Alzheimer's disease with plaques and tangles: Intracellular Abeta and synaptic dysfunction. *Neuron*. 2003;39(3):409–421.
19. Selkoe DJ. Soluble oligomers of the amyloid beta-protein impair synaptic plasticity and behavior. *Behav Brain Res*. 2008; 192(1):106–113.
20. Walsh DM, Klyubin I, Fadeeva JV, *et al*. Naturally secreted oligomers of amyloid beta protein potently inhibit hippocampal long-term potentiation *in vivo*. *Nature*. 2002;416(6880):535–539.
21. Itoh A, Akaike T, Sokabe M, *et al*. Impairments of long-term potentiation in hippocampal slices of beta-amyloid-infused rats. *Eur J Pharmacol*. 1999;382(3):167–175.
22. Eichenbaum H, Yonelinas AP, Ranganath C. The medial temporal lobe and recognition memory. *Annu Rev Neurosci*. 2007; 30:123–l52.
23. Vargha-Khadem F, Gadian DG, Watkins KE, Connelly A, Van Paesschen W, Mishkin M. Differential effects of early hippocampal pathology on episodic and semantic memory. *Science*. 1997;277(5324):376–380.
24. Masdeu JC, Zubieta JL, Arbizu J. Neuroimaging as a marker of the onset and progression of Alzheimer's disease. *J Neurol Sci*. 2005;236(1–2):55–64.
25. Wu W, Small SA. Imaging the earliest stages of Alzheimer's disease. *Curr Alzheimer Res*. 2006;3(5):529–539.
26. Stranahan AM, Mattson MP. Selective vulnerability of neurons in layer II of the entorhinal cortex during aging and Alzheimer's disease. *Neural Plast*. 2010;2010:108190.
27. Miller MI, Ratnanather JT, Tward DJ, *et al*. Network neurodegeneration in Alzheimer's disease *via* MRI based shape diffeomorphometry and high-field atlasing. *Front Bioeng Biotechnol*. 2015;3:54.
28. Gomez-Isla T, Price JL, McKeel DW Jr, Morris JC, Growdon JH, Hyman BT. Profound loss of layer II entorhinal cortex neurons occurs in very mild Alzheimer's disease. *J Neurosci*. 1996;16(14): 4491–4500.
29. Scheff SW, Price DA, Schmitt FA, Mufson EJ. Hippocampal synaptic loss in early Alzheimer's disease and mild cognitive impairment. *Neurobiol Aging*. 2006;27(10):1372–1384.
30. Lazarov O, Lee M, Peterson DA, Sisodia SS. Evidence that synaptically released beta-amyloid accumulates as extracellular deposits in the hippocampus of transgenic mice. *J Neurosci*. 2002;22(22):9785–9793.
31. Sheng JG, Price DL, Koliatsos VE. Disruption of corticocortical connections ameliorates amyloid burden in terminal fields in a transgenic model of Aβ amyloidosis. *J Neurosci*. 2002;22(22): 9794–9799.
32. Lambert JC, Ibrahim-Verbaas CA, Harold D, *et al*. Meta-analysis of 74,046 individuals identifies 11 new susceptibility loci for Alzheimer's disease. *Nat Genet*. 2013;45-(12):1452–1458.
33. Zhang B, Gaiteri C, Bodea LG, *et al*. Integrated systems approach identifies genetic nodes and networks in late-onset Alzheimer's disease. *Cell*. 2013;153(3):707–720.
34. Guerreiro R, Wojtas A, Bras J, *et al*. TREM2 variants in Alzheimer's disease. *N Engl J Med*. 2013;368(2):117–127.
35. Jonsson T, Stefansson H, Steinberg S, *et al*. Variant of TREM2 associated with the risk of Alzheimer's disease. *N Engl J Med*. 2013;368(2):107–116.
36. Efthymiou AG, Goate AM. Late onset Alzheimer's disease genetics implicates microglial pathways in disease risk. *Mol Neurodegener*. 2017;12(1):43.
37. Villegas-Llerena C, Phillips A, Garcia-Reitboeck P, Hardy J, Pocock JM. Microglial genes regulating neuroinflammation in the progression of Alzheimer's disease. *Curr Opin Neurobiol*. 2016;36:74–81.
38. Heneka MT, Carson MJ, El Khoury J, *et al*. Neuroinflammation in Alzheimer's disease. *Lancet Neurol*. 2015;14(4):388–405.
39. Calsolaro V, Edison P. Neuroinflammation in Alzheimer's disease: Current evidence and future directions. *Alzheimers Dement*. 2016;12(6):719–732.
40. Welikovitch LA, Do Carmo S, Maglóczky Z, *et al*. Early intraneuronal amyloid triggers neuron-derived inflammatory signaling in APP transgenic rats and human brain. *Proc Natl Acad Sci USA*. 2020;117(12):6844–6854.
41. Hong S, Beja-Glasser VF, Nfonoyim BM, *et al*. Complement and microglia mediate early synapse loss in Alzheimer mouse models. *Science*. 2016;352(6286):712–716.
42. Joshi P, Turola E, Ruiz A, *et al*. Microglia convert aggregated amyloid-beta into neurotoxic forms through the shedding of microvesicles. *Cell Death Differ*. 2014;21(4):582–593.
43. Gouwens LK, Ismail MS, Rogers VA, *et al*. Abeta42 protofibrils interact with and are trafficked through microglial-derived microvesicles. *ACS Chem Neurosci*. 2018;9(6):1416–1425.
44. Asai H, Ikezu S, Tsunoda S, *et al*. Depletion of microglia and inhibition of exosome synthesis halt tau propagation. *Nat Neurosci*. 2015;18(11):1584–1593.
45. Crotti A, Sait HR, McAvoy KM, *et al*. BIN1 favors the spreading of Tau *via* extracellular vesicles. *Sci Rep*. 2019;9(1):9477.
46. Ruan Z, Delpech JC, Venkatesan Kalavai S, *et al*. P2RX7 inhibitor suppresses exosome secretion and disease phenotype in P301S tau transgenic mice. *Mol Neurodegener*. 2020; 15(1):47.
47. Chivet M, Javalet C, Laulagnier K, Blot B, Hemming FJ, Sadoul R. Exosomes secreted by cortical neurons upon glutamatergic synapse activation specifically interact with neurons. *J Extracell Vesicles*. 2014;3:24722.
48. Koles K, Nunnari J, Korkut C, *et al*. Mechanism of evenness interrupted (Evi)-exosome release at synaptic boutons. *J Biol Chem*. 2012;287(20):16820–16834.

49. Bianco F, Perrotta C, Novellino L, *et al*. Acid sphingomyelinase activity triggers microparticle release from glial cells. *EMBO J*. 2009;28(8):1043–1054.
50. Picciolini S, Gualerzi A, Carlomagno C, *et al*. An SPRi-based biosensor pilot study: Analysis of multiple circulating extracellular vesicles and hippocampal volume in Alzheimer's disease. *J Pharm Biomed Anal*. 2021;192:113649.
51. Eitan E, Hutchison ER, Marosi K, *et al*. Extracellular vesicle-associated Aβ mediates trans-neuronal bioenergetic and Ca^{2+}-handling deficits in Alzheimer's disease models. *NPJ Aging Mech Dis*. 2016;2:16019.
52. Thery C, Witwer KW, Aikawa E, *et al*. Minimal information for studies of extracellular vesicles 2018 (MISEV2018): A position statement of the international society for extracellular vesicles and update of the MISEV2014 guidelines. *J Extracell Vesicles*. 2018;7(1):1535750.
53. Agosta F, Dalla Libera D, Spinelli EG, *et al*. Myeloid microvesicles in cerebrospinal fluid are associated with myelin damage and neuronal loss in mild cognitive impairment and Alzheimer disease. *Ann Neurol*. 2014;76(6):813–825.
54. D'Arrigo G, Gabrielli M, Scaroni F, *et al*. Astrocytes-derived extracellular vesicles in motion at the neuron surface: Involvement of the prion protein. *J Extracell Vesicles*. 2021;10(9):e12114.
55. Gabrielli M, Battista N, Riganti L, *et al*. Active endocannabinoids are secreted on extracellular membrane vesicles. *EMBO Rep*. 2015;16(2):213–220.
56. Podlisny MB, Ostaszewski BL, Squazzo SL, *et al*. Aggregation of secreted amyloid beta-protein into sodium dodecyl sulfate-stable oligomers in cell culture. *J Biol Chem*. 1995;270(16):9564–9570.
57. Prada I, Gabrielli M, Turola E, *et al*. Glia-to-neuron transfer of miRNAs *via* extracellular vesicles: A new mechanism underlying inflammation-induced synaptic alterations. *Acta Neuropathol*. 2018;135(4):529–550.
58. Zendrini A, Paolini L, Busatto S, *et al*. Augmented COlorimetric NANoplasmonic (CONAN) method for grading purity and determine concentration of EV microliter volume solutions. *Front Bioeng Biotechnol*. 2019;7:452.
59. Bianco F, Pravettoni E, Colombo A, *et al*. Astrocyte-derived ATP induces vesicle shedding and IL-1 beta release from microglia. *J Immunol*. 2005;174(11):7268–7277.
60. Osteikoetxea X, Sódar B, Nemeth A, *et al*. Differential detergent sensitivity of extracellular vesicle subpopulations. *Org Biomol Chem*. 2015;13(38):9775–9782.
61. Prada I, Amin L, Furlan R, Legname G, Verderio C, Cojoc D. A new approach to follow a single extracellular vesicle–cell interaction using optical tweezers. *Biotechniques*. 2016;60(1):35–41.
62. Brenna S, Altmeppen HC, Mohammadi B, *et al*. Characterization of brain-derived extracellular vesicles reveals changes in cellular origin after stroke and enrichment of the prion protein with a potential role in cellular uptake. *J Extracell Vesicles*. 2020;9(1):1809065.
63. Origlia N, Capsoni S, Cattaneo A, *et al*. Aβ-dependent Inhibition of LTP in different intracortical circuits of the visual cortex: The role of RAGE. *J Alzheimers Dis*. 2009;17(1):59–68.
64. Criscuolo C, Fontebasso V, Middei S, *et al*. Entorhinal cortex dysfunction can be rescued by inhibition of microglial RAGE in an Alzheimer's disease mouse model. *Sci Rep*. 2017;7:42370.
65. Origlia N, Bonadonna C, Rosellini A, *et al*. Microglial receptor for advanced glycation end product-dependent signal pathway drives beta-amyloid-induced synaptic depression and long-term depression impairment in entorhinal cortex. *J Neurosci*. 2010;30(34):11414–11425.
66. Origlia N, Righi M, Capsoni S, *et al*. Receptor for advanced glycation end product-dependent activation of p38 mitogen-activated protein kinase contributes to amyloid-beta-mediated cortical synaptic dysfunction. *J Neurosci*. 2008;28(13):3521–3530.
67. Ziehm T, Brener O, van Groen T, *et al*. Increase of positive net charge and conformational rigidity enhances the efficacy of D-enantiomeric peptides designed to eliminate cytotoxic abeta species. *ACS Chem Neurosci*. 2016;7(8):1088–1096.
68. Kasai H, Matsuzaki M, Noguchi J, Yasumatsu N, Nakahara H. Structure–stability–function relationships of dendritic spines. *Trends Neurosci*. 2003;26(7):360–368.
69. Lu W, Man H, Ju W, Trimble WS, MacDonald JF, Wang YT. Activation of synaptic NMDA receptors induces membrane insertion of new AMPA receptors and LTP in cultured hippocampal neurons. *Neuron*. 2001;29(1):243–254.
70. Fossati G, Morini R, Corradini I, *et al*. Reduced SNAP-25 increases PSD-95 mobility and impairs spine morphogenesis. *Cell Death Differ*. 2015;22(9):1425–1436.
71. Antonucci F, Turola E, Riganti L, *et al*. Microvesicles released from microglia stimulate synaptic activity *via* enhanced sphingolipid metabolism. *EMBO J*. 2012;31(5):1231–1240.
72. Bliss TV, Collingridge GL. A synaptic model of memory: Long-term potentiation in the hippocampus. *Nature*. 1993;361(6407):31–39.
73. Liu L, Drouet V, Wu JW, *et al*. Trans-synaptic spread of tau pathology *in vivo*. *PLoS One*. 2012;7(2):e31302.
74. Tamamaki N, Nojyo Y. Projection of the entorhinal layer II neurons in the rat as revealed by intracellular pressure-injection of neurobiotin. *Hippocampus*. 1993;3(4):471–480.
75. Lombardi M, Parolisi R, Scaroni F, *et al*. Detrimental and protective action of microglial extracellular vesicles on myelin lesions: Astrocyte involvement in remyelination failure. *Acta Neuropathol*. 2019;138(6):987–1012.
76. Yiannopoulou KG, Papageorgiou SG. Current and future treatments for Alzheimer's disease. *Ther Adv Neurol Disord*. 2013;6(1):19–33.
77. Godyn J, Jończyk J, Panek D, Malawska B. Therapeutic strategies for Alzheimer's disease in clinical trials. *Pharmacol Rep*. 2016;68(1):127–138.
78. Wang H-W, Pasternak JF, Kuo H, *et al*. Soluble oligomers of beta amyloid (1-42) inhibit long-term potentiation but not long-term depression in rat dentate gyrus. *Brain Res*. 2002;924(2):133–140.
79. Palop JJ, Mucke L. Amyloid-beta-induced neuronal dysfunction in Alzheimer's disease: From synapses toward neural networks. *Nat Neurosci*. 2010;13(7):812–818.
80. Wang Y, Balaji V, Kaniyappan S, *et al*. The release and trans-synaptic transmission of Tau *via* exosomes. *Mol Neurodegener*. 2017;12(1):5.
81. Sardar Sinha M, Ansell-Schultz A, Civitelli L, *et al*. Alzheimer's disease pathology propagation by exosomes containing toxic amyloid-beta oligomers. *Acta Neuropathol*. 2018;136(1):41–56.
82. Polanco JC, Li C, Durisic N, Sullivan R, Gotz J. Exosomes taken up by neurons hijack the endosomal pathway to spread to interconnected neurons. *Acta Neuropathol Commun*. 2018;6(1):10.
83. De Strooper B, Karran E. The cellular phase of Alzheimer's disease. *Cell*. 2016;164(4):603–615.
84. Jarosz-Griffiths HH, Noble E, Rushworth JV, Hooper NM. Amyloid-beta receptors: The good, the bad, and the prion protein. *J Biol Chem*. 2016;291(7):3174–3183.
85. Mroczko B, Groblewska M, Litman-Zawadzka A, Kornhuber J, Lewczuk P. Cellular receptors of amyloid beta oligomers

(AbetaOs) in Alzheimer's disease. *Int J Mol Sci*. 2018;19(7):1884.
86. Arancio O, Zhang HP, Chen X, *et al*. RAGE potentiates Abeta-induced perturbation of neuronal function in transgenic mice. *EMBO J*. 2004;23(20):4096–4105.
87. Roy ER, Wang B, Wan YW, *et al*. Type I interferon response drives neuroinflammation and synapse loss in Alzheimer disease. *J Clin Invest*. 2020;130(4):1912–1930.
88. Martins IC, Kuperstein I, Wilkinson H, *et al*. Lipids revert inert Abeta amyloid fibrils to neurotoxic protofibrils that affect learning in mice. *EMBO J*. 2008;27(1):224–233.
89. Johansson AS, Garlind A, Berglind-Dehlin F, *et al*. Docosahexaenoic acid stabilizes soluble amyloid-beta protofibrils and sustains amyloid-beta-induced neurotoxicity *in vitro*. *FEBS J*. 2007;274(4):990–1000.
90. Ruan Z, Pathak D, Venkatesan Kalavai S, *et al*. Alzheimer's disease brain-derived extracellular vesicles spread tau pathology in interneurons. *Brain*. 2021;144(1):288–309.
91. Chiarini A, Armato U, Gardenal E, Gui L, Dal Pra I. Amyloid beta-exposed human astrocytes overproduce phospho-tau and overrelease it within exosomes, effects suppressed by calcilytic NPS 2143-further implications for Alzheimer's therapy. *Front Neurosci*. 2017;11:217.
92. Guix FX, Corbett GT, Cha DJ, *et al*. Detection of aggregation-competent tau in neuron-derived extracellular vesicles. *Int J Mol Sci*. 2018;19(3):663.
93. Söllvander S, Nikitidou E, Brolin R, *et al*. Accumulation of amyloid-beta by astrocytes result in enlarged endosomes and microvesicle-induced apoptosis of neurons. *Mol Neurodegener*. 2016;11(1):38.
94. Beretta C, Nikitidou E, Streubel-Gallasch L, Ingelsson M, Sehlin D, Erlandsson A. Extracellular vesicles from amyloid-beta exposed cell cultures induce severe dysfunction in cortical neurons. *Sci Rep*. 2020;10(1):19656.
95. van Niel G, D'Angelo G, Raposo G. Shedding light on the cell biology of extracellular vesicles. *Nat Rev Mol Cell Biol*. 2018;19(4):213–228.
96. Verweij FJ, Hyenne V, Van Niel G, Goetz JG. Extracellular vesicles: Catching the light in zebrafish. *Trends Cell Biol*. 2019;29(10):770–776.
97. Heusermann W, Hean J, Trojer D, *et al*. Exosomes surf on filopodia to enter cells at endocytic hot spots, traffic within endosomes, and are targeted to the ER. *J Cell Biol*. 2016;213(2):173–184.
98. Amin L, Nguyen XTA, Rolle IG, *et al*. Characterization of prion protein function by focal neurite stimulation. *J Cell Sci*. 2016;129(20):3878–3891.
99. Nguyen XTA, Tran TH, Cojoc D, Legname G. Copper binding regulates cellular prion protein function. *Mol Neurobiol*. 2019;56(9):6121–6133.
100. French KC, Antonyak MA, Cerione RA. Extracellular vesicle docking at the cellular port: Extracellular vesicle binding and uptake. *Semin Cell Dev Biol*. 2017;67:48–55.
101. Buzás EI, Tóth EA, Sódar BW, Szabo-Taylor KE. Molecular interactions at the surface of extracellular vesicles. *Semin Immunopathol*. 2018;40(5):453–464.
102. Arab T, Raffo-Romero A, Van Camp C, *et al*. Proteomic characterisation of leech microglia extracellular vesicles (EVs): Comparison between differential ultracentrifugation and Optiprep™ density gradient isolation. *J Extracell Vesicles*. 2019;8(1):1603048.
103. Weinhard L, di Bartolomei G, Bolasco G, *et al*. Microglia remodel synapses by presynaptic trogocytosis and spine head filopodia induction. *Nat Commun*. 2018;9(1):1228.